NIRS-M-261

NIRS Workshop on PET Imaging Physics and Applications

PIPA2013

Abstract Book

Nov. 4 - 5, 2013
PACIFICO Yokohama, Japan

Host organization:
National Institute of Radiological Sciences

NIRS Workshop on PET Imaging Physics and Applications (PIPA2013)

Date / Venue: Nov. 4 - 5, 2013 / PACIFICO Yokohama (Conference Center, Room 315), Japan
Host organization: National Institute of Radiological Sciences

Day 1: Nov. 4 Mon., 2013

12:30	(Registration open)	
13:30	Opening speech	Yoshiharu Yonekura (NIRS President)
13:40	PET physics research at NIRS	Taiga Yamaya (NIRS)

Special lecture Chair: Yasuhisa Fujibayashi (NIRS)

14:20	Theranostics: A future of personalized nuclear medicine	Tomio Inoue (Yokohama City University)

15:00 Group photo & Coffee break (30 min)

Plenary talks Chair: Katsuyuki Taguchi (Johns Hopkins University School of Medicine)

15:30	Session highlights in Japanese 日本語による基礎解説	Katsuyuki Taguchi (Johns Hopkins University School of Medicine)
15:40	(invited) Detector and electronics development at the University of Washington	Thomas K. Lewellen (University of Washington)
16:20	(invited) Ultimate time resolution in TOF PET scanners	Paul Lecoq (CERN)
17:00	(invited) The development and applications of a small animal simultaneous SPECT/MR imaging system	Benjamin M. W. Tsui (Johns Hopkins University)

18:00 Reception (to be charged)

Day 2: Nov. 5 Tue., 2013

Imaging in particle therapy -1 Chair: Taku Inaniwa (NIRS)

8:00	(Registration open)	
8:30	Session highlights in Japanese 日本語による基礎解説	Taku Inaniwa (NIRS)
8:40	Medical application of radioisotope beams and trials at HIMAC	Atsushi Kitagawa (NIRS)
9:10	Offline PET-based treatment verification at the Heidelberg Ion-Beam Therapy Center: clinical experience and on-going research	Christopher Kurz (Heidelberg University Hospital)
9:30	Development of data acquisition system for the human OpenPET	Eiji Yoshida (NIRS)

9:45 Short break (15 min)

Imaging in particle therapy -2 Chair: Taiga Yamaya (NIRS)

10:00	Session highlights in Japanese 日本語による基礎解説	Taiga Yamaya (NIRS)
10:10	(invited) Time-of-Flight PET in clinical and application-specific imaging	Suleman Surti (University of Pennsylvania)
10:40	Evaluation of open-ring imaging systems for range verification in proton-therapy by means of secondary radiation	Irene Torres-Espallardo (University of Valencia)
11:00	Development of a three layer Compton telescope prototype based on continuous LaBr3 crystals and silicon photomultipliers	Marco Trovato (University of Valencia)
11:20	Real-time OpenPET imaging system toward PET-guided tumor tracking radiation therapy	Hideaki Tashima (NIRS)
11:35	Performance improvement of GPU image reconstruction for OpenPET	Haruhiko Futada (Mizuho Info. & Res. Inst.)

11:50 Break (90 min)

Detectors and systems Chair: Hideo Murayama

13:20	Session highlights in Japanese 日本語による基礎解説	Hideo Murayama
13:30	(invited) Time-based pulse signal processing and multiplexing method for frontend electronics	Hiroyuki Takahashi (University of Tokyo)
14:00	(invited) Recent results in SiPM-based detectors for time-of-flight PET and their promise for in-beam PET and prompt gamma ray imaging	Dennis R. Schaart (Delft University of Technology)
14:30	X'tal cube: 3-dimensional position sensitive PET detector	Naoko Inadama (NIRS)
14:50	An asymmetric PQS detector-block design for a gapless PET detector ring	Wai-Hoi Wong (University of Texas)
15:10	MuPET images of anesthetized healthy mice under different conditions	Hossain Baghaei (University of Texas)
15:25	Enhanced scintillation crystals through co-doping and growth improvements	Daniel J. Herr (Saint-Gobain Recherche)

15:40 Coffee break (30 min)

Multimodal imaging and reconstruction Chair: Iwao Kanno (NIRS)

16:10	Session highlights in Japanese 日本語による基礎解説	Iwao Kanno (NIRS)
16:20	(invited) VECTor+: Quarter mm, quarter minute & quarter MBq quantitative total body SPECT, with simultaneous 3-quarter-mm PET & 2-quarter-mm SPECT capability	Freek Beekman (Delft University of Technology / MILabs)
16:50	(invited) Development of molecular imaging systems and applications	Seiichi Yamamoto (Nagoya University)
17:20	Development of a removable MR head coil integrated with high resolution PET detectors	Takayuki Obata (NIRS)
17:40	First experience with a novel preclinical PET/CT scanner with stationary/rotating detector	Nicola Belcari (University of Pisa/INFN Pisa)

18:00 Closing remarks — Makoto Akashi (NIRS Executive Director)

NIRS Workshop on PET Imaging Physics and Applications (PIPA2013)

Date	Nov. 4 - 5, 2013	
Venue	PACIFICO Yokohama, Japan	
Host organization	National Institute of Radiological Sciences	
Cosponsors	Chiba University Research Center for Frontier Medical Engineering	国立大学法人千葉大学 フロンティア医工学センター
	City of Yokohama	横浜市
	IEEE NPSS Japan Chapter	IEEE NPSS Japan Chapter
	Japan Radioisotope Association	公益社団法人日本アイソトープ協会
	Japan Society of Applied Physics	公益社団法人応用物理学会
	Japan Society of Medical Physics	一般社団法人日本医学物理学会
	Japanese Society for Magnetic Resonance in Medicine	一般社団法人日本磁気共鳴医学会
	Japanese Society for Molecular Imaging	日本分子イメージング学会
	Japanese Society of Medical Imaging Technology	日本医用画像工学会
	Japanese Society of Nuclear Medicine	一般社団法人日本核医学会
	The 186th Committee on Radiation Science and Its Applications in the Japan Society for the Promotion of Science	独立行政法人日本学術振興会 放射線科学とその応用第186委員会
	Yokohama Convention & Visitors Bureau	公益財団法人横浜観光コンベンション・ビューロー
Chair organizer	Taiga Yamaya	National Institute of Radiological Sciences

Local Organization Committee

Hiroshi Ito, Yoko Ikoma, Naoko Inadama, Taku Inaniwa, Iwao Kanno, Hiroshi Kawaguchi, Fumihiko Nishikido, Takayuki Obata, Eiji Yoshida	National Institute of Radiological Sciences

International Advisory Committee

Tomoyuki Hasegawa	Kitasato University
Hidehiro Iida	National Cerebral and Cardiovascular Center
Tomio Inoue	Yokohama City University
Ikuo Kanno	Kyoto University
Paul Kinahan	University of Washington
Jae Sung Lee	Seoul National University
Craig Levin	Stanford University
Stan Majewski	West Virginia University
Robert Miyaoka	University of Washington
Takashi Obi	Tokyo Institute of Technology
Koichi Ogawa	Housei University
Katia Parodi	Ludwig-Maximilians-University in Munich
Anatoly Rozenfeld	University of Wollongong
Suleman Surti	University of Pennsylvania
Katsuyuki Taguchi	Johns Hopkins University
Hiroyuki Takahashi	University of Tokyo
Hiroshi Watabe	Tohoku University
Seiichi Yamamoto	Nagoya University
Akira Yoshikawa	Tohoku University
Sibylle Ziegler	Technische Universität München

Table of Contents

		Page
(1) PET physics research at NIRS	T. Yamaya	1
(2) Theranostics: A future of personalized nuclear medicine	T. Inoue	4
(3) Detector and Electronics Development at the University of Washington	T. Lewellen, et al.	5
(4) Ultimate time resolution in TOF PET scanners	P. Lecoq	7
(5) The Development and Applications of a small animal simultaneous SPECT/MR imaging system	B. M. W. Tsui, et al.	9
(6) Medical application of radioisotope beams and trials at HIMAC	A. Kitagawa, et al.	11
(7) Offline PET-based Treatment Verification at the Heidelberg Ion-Beam Therapy Center: Clinical Experience and On-Going Research	C. Kurz, et al.	13
(8) Development of data acquisition system for the human OpenPET	E. Yoshida, et al.	15
(9) Time-of-Flight PET in clinical and application-specific imaging	S. Surti	17
(10) Evaluation of open-ring imaging systems for range verification in proton-therapy by means of secondary radiation	I. Torres-Espallardo, et al.	19
(11) Development of a Three Layer Compton Telescope Prototype Based on Continuous $LaBr_3$ Crystals and Silicon Photomultipliers	M. Trovato, et al.	21
(12) Real-time OpenPET imaging system toward PET-guided tumor tracking radiation therapy	H. Tashima, et al.	23
(13) Performance improvement of GPU image reconstruction for OpenPET	H. Futada, et al.	25
(14) Time-based pulse signal processing and multiplexing method for frontend electronics	H. Takahashi, et al.	27
(15) Recent results in SiPM-based detectors for Time-of-Flight PET and their promise for In-Beam PET and prompt gamma ray imaging	D.R. Schaart	29
(16) X'tal cube: 3-dimensional position sensitive PET detector	N. Inadama, et al.	31
(17) An asymmetric PQS detector-block design for a gapless PET detector ring	H. Li, et al.	33
(18) MuPET Images of Anesthetized Healthy Mice under Different Conditions	H. Baghaei, et al.	35
(19) Enhanced Scintillation Crystals Through Co-Doping and Growth Improvements	S. Blahuta, et al.	37
(20) VECTor$^+$:1/4 mm, 1/4 minute &1/4 MBq quantitative total body SPECT, with simultaneous 3/4-mm PET and 2/4-mm SPECT capability	F. Beekman, et al.	39
(21) Development of molecular imaging systems and applications	S. Yamamoto	41
(22) Development of a removable MR head coil integrated with high-resolution PET detectors	T. Obata, et al.	43
(23) First experience with a novel Preclinical PET/CT scanner with stationary/rotating detectors	N. Belcari	45

PET physics research at NIRS

Taiga Yamaya

Molecular Imaging Center, National Institute of Radiological Sciences, Japan

Positron emission tomography (PET) plays important roles in cancer diagnosis, neuroimaging and molecular imaging research; but potential points remain for which big improvements could be made, including spatial resolution, sensitivity and manufacturing costs. For example, the sensitivity of present PET scanners does not exceed 10%. This means that more than 90% of the gamma-rays emitted from a subject are not utilized for imaging. Therefore, research on next generation PET technologies remains a hot topic worldwide.

Since Dr. Eiichi Tanaka developed the first PET scanner in Japan in 1979, National Institute of Radiological Sciences (NIRS) has continued PET physics research in terms of radiation detectors, data acquisition systems, image reconstruction algorithms and data correction methods to improve image quality and quantity in nuclear medicine as well as exploring innovative systems. Dr. Taiga Yamaya has been a team leader since 2008 in succession to Dr. Hideo Murayama.

A depth-of-interaction (DOI) detector, for which various methods have been studied, will be a key device to get any significant improvement in sensitivity while maintaining high spatial resolution. Among them, we have developed 4-layered DOI detectors based on a light sharing method [1]. For a proof-of-concept, we have developed 120 detector blocks, each of which consists of 16 x 16 x 4 array of GSO crystals sized in 2.9 x 2.9 x 7.5 mm^3 (Hitachi Chemical) and a 256 channel flat panel multi-anode photomultiplier tube (PMT) (Hamamatsu H9500) [2]. Using these detector blocks, we have developed a brain PET scanner "jPET-D4", which has been showed to have almost uniform spatial resolution around 2mm for all over the field-of-view with iterative image reconstruction with geometrically defined system matrix [3]. We have also succeed to upgrade the DOI detector to have better spatial resolution with cheaper production costs [4][5]: successful identification of 32 x 32 x 4 array of LYSO crystals sized in 1.45 x 1.45 x 4.5 mm^3 with a 64ch PMT (Hamamatsu H8500), which has enabled Shimadzu's new products of positron emission mammography (PEM) [6]. It should be noted that DOI information has a potential to improve timing resolution for time-of-flight PET [7].

DOI measurement also has a potential to expand PET application fields because it allows for more flexible detector arrangement. As an example, we are developing the world's first, open-type PET geometry "OpenPET" [8], which is expected to lead to 1) PET imaging during treatment as well as 2) real-time multimodal imaging by inserting another imaging device in the gap and 3) extension of an axial FOV with a limited number of detectors [9]-[12].

Our main application of the OpenPET is PET-image guided particle therapy such as *in situ* dose verification and/or direct tumor tracking by means of PET [13][14]. Following our first idea of a dual-ring Open PET (DROP) [15], in the last year, we proposed our second-generation geometry, single-ring OpenPET (SROP), which is more efficient than the DROP in terms of a cost and sensitivity [16][17]. In this year, we developed a SROP prototype based on a novel detector arrangement, in which block detectors originally forming a conventional PET scanner were axially shifted little by little [18]. Sixteen detector units each of which consisted of two DOI detectors were arranged to form a perfect circle of 25cm in diameter. Detector units had an axial shifting mechanism to be transformed into the SROP so that the scanner can be used as a conventional (i.e., non-open) PET in the case that in-beam PET measurement is not essentially required. We carried out in-beam imaging tests in the Heavy Ion Medical Accelerator in Chiba (HIMAC). In addition to usual carbon (^{12}C) beam, we applied RI beams of ^{11}C and ^{10}C [19]. Stopping position of primary particles was directly imaged with the RI beam irradiation, while distribution of secondary particles was imaged with the ^{12}C beam irradiation.

The DOI detector itself continues to evolve with the help of recently developed semiconductor photodetectors, often referred to as silicon photomultipliers (SiPMs). We are developing a SiPM-based DOI detector "X'tal cube" [20]-[22] to achieve sub-mm spatial resolution, which is reaching the theoretical limitation of PET imaging. We have developed a prototype of 1mm isotropic detector resolution with Multi-Pixel Photon Counters (Hamamatsu), which equals the world record [23]. Because SiPMs are almost insensitive to strong magnetic field, this detector promises a high-resolution integrated PET/MRI.

References

[1] H. Murayama, et al., "Depth encoding multicrystal detectors for PET," IEEE Trans. Nucl. Sci., 45, p. 1152, 1998.

[2] N. Inadama, et al., "A depth of interaction detector for PET with GSO crystals doped with different amounts of Ce," IEEE Trans. Nucl. Sci., 49, p. 629, 2002.

[3] T. Yamaya, et al., "First human brain imaging by the jPET-D4 prototype with a pre-computed system matrix," IEEE Trans. Nucl. Sci., 55, p. 2482, 2008.

[4] N. Inadama, et al., "8-layer DOI encoding of 3-dimensional crystal array," IEEE Trans. Nucl. Sci., 53, p. 2523, 2006.

[5] T. Tsuda, et al., "A four-layer depth of interaction detector block for small animal PET," IEEE Trans. Nucl. Sci. 51, p. 2537, 2004.

[6] K. Kitamura, et al., "Development of a C-shaped breast PET scanner equipped with four-layer DOI detectors," Conf. Rec. 2008 IEEE NSS-MIC, 2008.

[7] K. Shibuya, et al., "Timing resolution improvement using DOI information in a four-layer scintillation

detector for TOF-PET," Nuclear Instruments and Methods in Physics Research A 593, p. 572, 2008.
[8] T. Yamaya, et al., "A proposal of an open PET geometry," Phy. Med. Biol., 53, p. 757, 2008.
[9] T. Yamaya, et al, "Imaging simulations of an "OpenPET" geometry with shifting detector rings," Radiol. Phys. Technol., 2, p. 62, 2009.
[10] T. Yamaya, et al., "Simulation studies of a new 'OpenPET' geometry based on a quad unit of detector rings," Phys. Med. Biol., 54, p. 1223, 2009.
[11] T. Yamaya, et al., "A multiplex "OpenPET" geometry to extend axial FOV without increasing the number of detectors," IEEE Trans. Nucl. Sci., 56, p. 2644, 2009.
[12] E. Yoshida, et al., "Feasibility study of an axially extendable multiplex cylinder PET," IEEE Trans. Nucl. Sci., 60, p. 3227, 2013.
[13] H. Tashima, "Real-time imaging system for the OpenPET," IEEE Trans. Nucl. Sci., 59, p. 40, 2012.
[14] S. Kinouchi, et al., "GPU-based PET image reconstruction using an accurate geometrical system model," IEEE Trans. Nucl. Sci., 59, p. 1977, 2012.
[15] T. Yamaya, et al., "Development of a small prototype for a proof-of-concept of OpenPET imaging," Phys. Med. Biol., 56, p. 1123, 2011.
[16] H. Tashima , et al., "A single-ring OpenPET enabling PET imaging during radiotherapy," Phys. Med. Biol. 57, p. 4705, 2012.
[17] E. Yoshida, et al., "Development of a single-ring OpenPET prototype," Nuclear Instruments and Methods in Physics Research A, 729, p. 800, 2013.
[18] T. Yamaya, et al, "A prototype of a novel transformable single-ring OpenPET," 2013 IEEE NSS-MIC, M07-2, 2013.
[19] E. Urakabe, et al., "Spot scanning using radioactive ^{11}C beams for heavy-ion radiotherapy," Jpn. J. Appl. Phys., 40, p. 2540, 2001.
[20] Y. Yazaki, et al., "Development of the X'tal cube: a 3D position-sensitive radiation detector with all-surface MPPC readout," IEEE Trans. Nucl. Sci., 59, p. 462, 2012.
[21] E. Yoshida, et al., "The X'tal cube PET detector with a monolithic crystal processed by the 3D sub-surface laser engraving technique: Performance comparison with glued crystal elements," Nuclear Instruments and Methods in Physics Research A 723, p. 83, 2013.
[22] Y. Hirano, et al., "Potential for reducing the numbers of SiPM readout surfaces of laser-processed X'tal cube PET detectors," Phys. Med. Biol. 58, p. 1361, 2013.
[23] T. Yamaya, et al., "A SiPM-based isotropic-3D PET detector X'tal cube with a three-dimensional array of 1 mm^3 crystals," Phys. Med. Biol., 56, p. 6793, 2011.

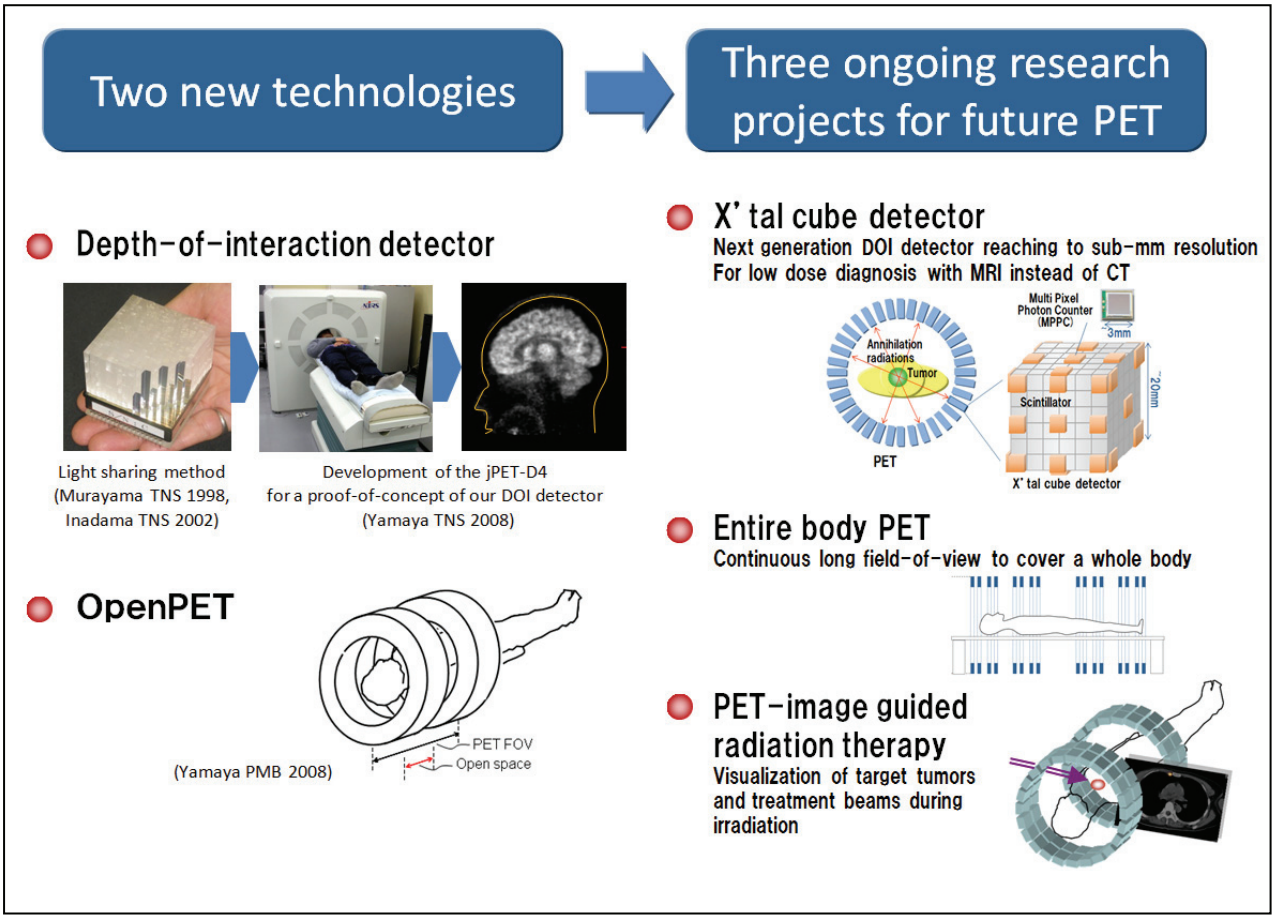

OpenPET: full-ring in-beam PET

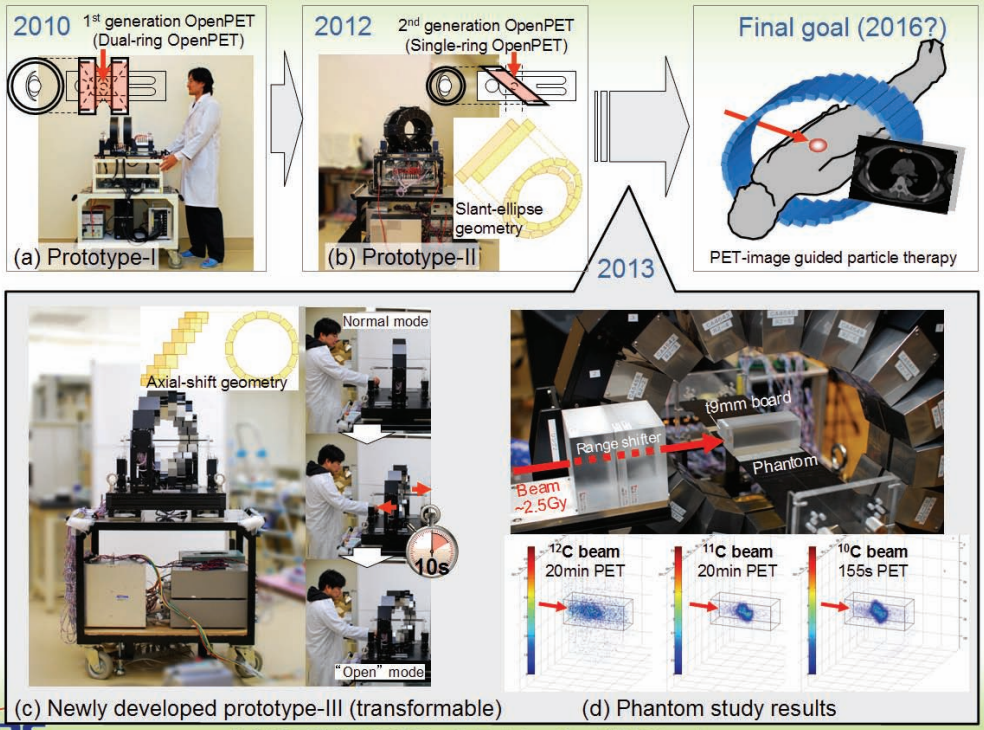

"X' tal cube": SiPM-based isotropic-3D detector

- Light sharing
  - Higher resolution than photodetector resolution
- A segmented crystal array with no reflector insertion
  - Uniform crystal identification performance with the Anger-type calculation
- Full-face detection of scintillation photons
  - Efficient light detection, thus expecting better spatial, energy and timing resolution.

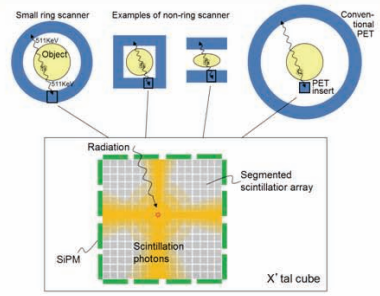

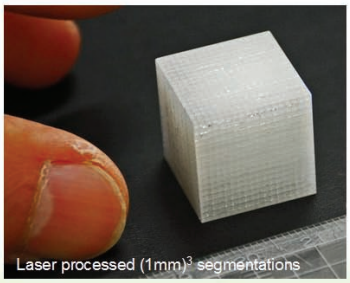

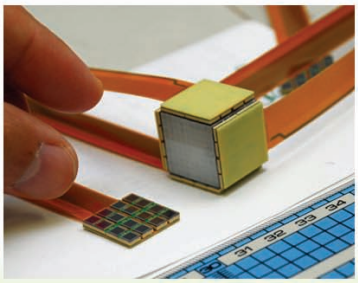

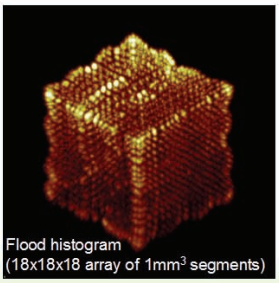

Theranostics: A future of personalized nuclear medicine

Tomio Inoue MD
Department of Radiology
Yokohama City University School of Medicine

The Japanese Society of Nuclear Medicine (JSNM) was established in 1964, of which main purpose is the appropriate development for clinical application of radioactive substances and stable nuclide in medicine. JSNM currently has about 3500 members, comprising physicians, physicists, chemists, pharmacists, technologists, and others interested in the clinical and investigational use of radiopharmaceuticals. Every five years nation-wide survey of nuclear medicine in Japan presented a trend to increase in number of PET and radionuclide (RN) internal therapy while dramatically decrease in number of conventional nuclear medicine examinations. These data means that PET as molecular imaging and RN internal therapy will be important in the field of nuclear medicine in Japan. JSNM established two special strategic committees for facilitating these two topics as therapy and diagnosis. Molecular imaging strategic committee has been working positively to generate academic cGMP guidance for in-house PET radiopharmaceutical production, preclinical guidance, and clinical guidance for clinical PET study, and trying to establish auditing system for keeping high quality of PET pharmaceutical generated by in-house auto-synthetic devices and image quality of clinical PET study. Strategic committee for radionuclide therapy has generated a draft of guideline and future proposal plan for facilitating radionuclide therapy in Japan. A concept for diagnosis connected with therapy is so-called “Theranostics”; one of the most successful example is a patient’s selection of Her2 positive breast cancer by immunehistochemical pathological diagnosis for molecular target therapy by trastuzumab; monoclonal antibody that binds to her2 (human epidermal growth factor 2). In the field of nuclear medicine, a diagnosis with PET/CT, PET/MR or positron emission mammography (PEM) connected with molecular target therapy or radiation therapy including internal radionuclide therapy has a potential for conducting personalized nuclear medicine.

Detector and Electronics Development at the University of Washington

Tom Lewellen[1], Robert Miyoaka[1]

[1] University of Washington, UA

Our laboratory has several depth-of-interaction detector design projects underway targeted at specific applications. These projects also lead to problems in adapting existing data acquisition electronics to the requirements for these new devices. In this paper we will provide an overview of three major detector projects and the supporting electronics system we have developed for the detectors. There are four major detector projects underway – all characterized by placing photosensors only on one surface of the crystal or crystal array (Figure 1). Two are based on monolithic crystals viewed by arrays of silicon photomultipliers or multi-anode photomultiplier tubes. The cMiCE places the photosensors on the surface of the crystal opposite to the incoming gamma rays, while the SES variant places the photosensors on the "front" face of the crystal. Our paired crystal approach (dMiCE) which uses controlled light sharing to decode depth. To make such an approach practical, we have explored sub surface laser etching to provide the required variable light-sharing interface. Finally, we have developed a hybrid between the monolithic and discrete crystal approaches that uses slats of crystals (TSC).

To support these detectors, we have also developed a basic building block for acquisition electronics that moves the majority of all the pulse processing into field programmable gate arrays (FPGA) [1,2]. This board, which we term our Phase II board, is very flexible and able to support complex tasks such as performing statistical estimation of event positions in x,y, and z in addition to pulse integration, timing (using a fitted model pulse approach), baseline restoration, and pulse pile-up correction. The board includes 64 channels of 65 mHz ADCs and one high speed ADC (currently 350 mHz). The 64 ADC channels can be converted to 64 channels of high speed serial input to support detectors that are capable of sending out digital data instead of analog data (such as the Philips digital SiPM system). Figure 2 depicts a basic logic configuration of the board to support the cMiCE detector design. The connection to the host computer is currently USB 3 but the board can be configured to support other interfaces such as FireWire and PCIe. In this case, the high speed ADC channel is used with a timing pickoff signal from the multi-channel PMT and is processed for pileup correction and pulse fitting to extract the time of the event. The other 64 channels are also corrected for pileup and baseline and then integrated and processed to use the signals form the individual sensors to estimate the event position. Finally, under the direction of an embedded processor implemented within the FPGA logic, the data is packaged and sent to the host computer.

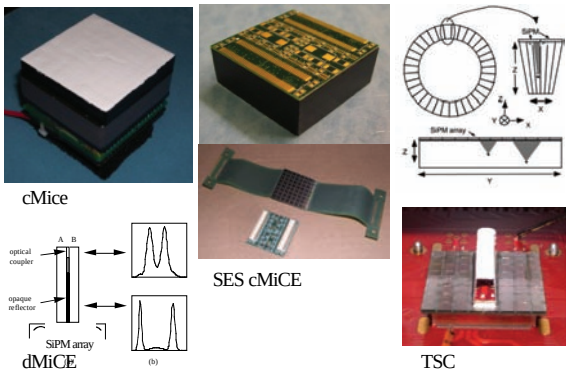

Figure 1: The four basic detector types currently being developed at the University of Washington (cMiCE, SES, dMiCE and TSC).

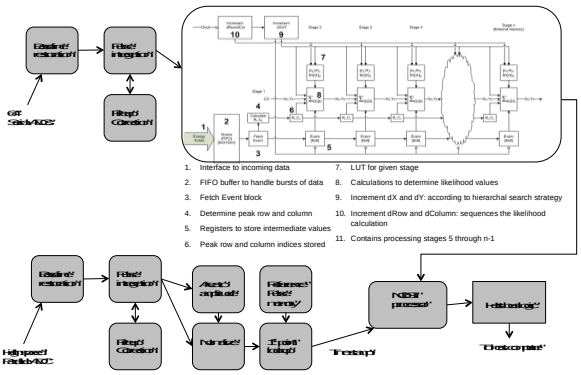

Figure 2: Diagram of the basic FPGA logic used for the cMICE detector.

The Phase II boards can be grouped together to implement a wide range of acquisition topologies. To further enhance the flexibility of the board, expansion connectors are provided to allow a user to add additional hardware features the base boards may not provide.

References

[1] Li, X., Hunter, W.C.J., Lewellen, T.K., Miyaoka, R.S.: "Spatial Resolution Performance Evaluation for a Monolithic Crystal PET Detector with Cramer-Rao Lower Bound", IEEE Nuclear Science Symposium and Medical Imaging Conference, pp. 2202-2205 (2010).

[2] DeWitt, D., Miyaoka, R.S., Xiaoli, Li, Lockhart, C., Lewellen, T.K., Hauck, S.: "Design of an FPGA based algorithm for real-time solutions of Statistics-Based Positioning", Trans. Nucl. Sci. vol 57(1): pp. 2769-2776 (2010).

Current UW Detector Designs

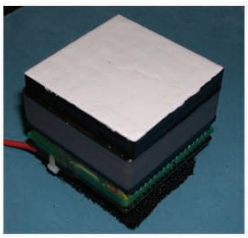

cMiCE - 64 channel readout

photons

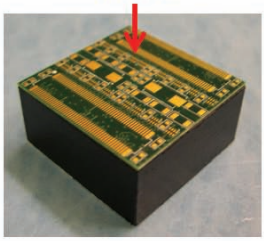

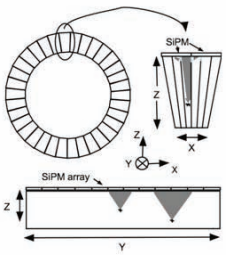

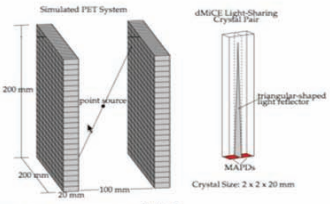

Figure 1

dMiCE – 40+ channel readout, SSLE used to put light sharing pattern into crystals

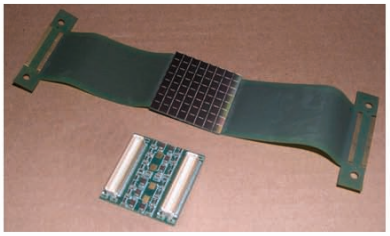

SES cMiCE - 64 channel readout*

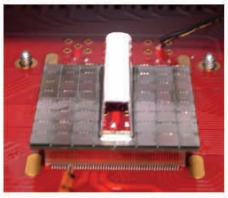

TSC detector – 2 by 8 (or 12) channel readout**

All of the designs are being supported by our new electronics system based on our Phase II digital board and a new row/column + timing pickoff ASIC for SiPM devices

Phase II electronics example - FPGA tool set for UW cMiCE

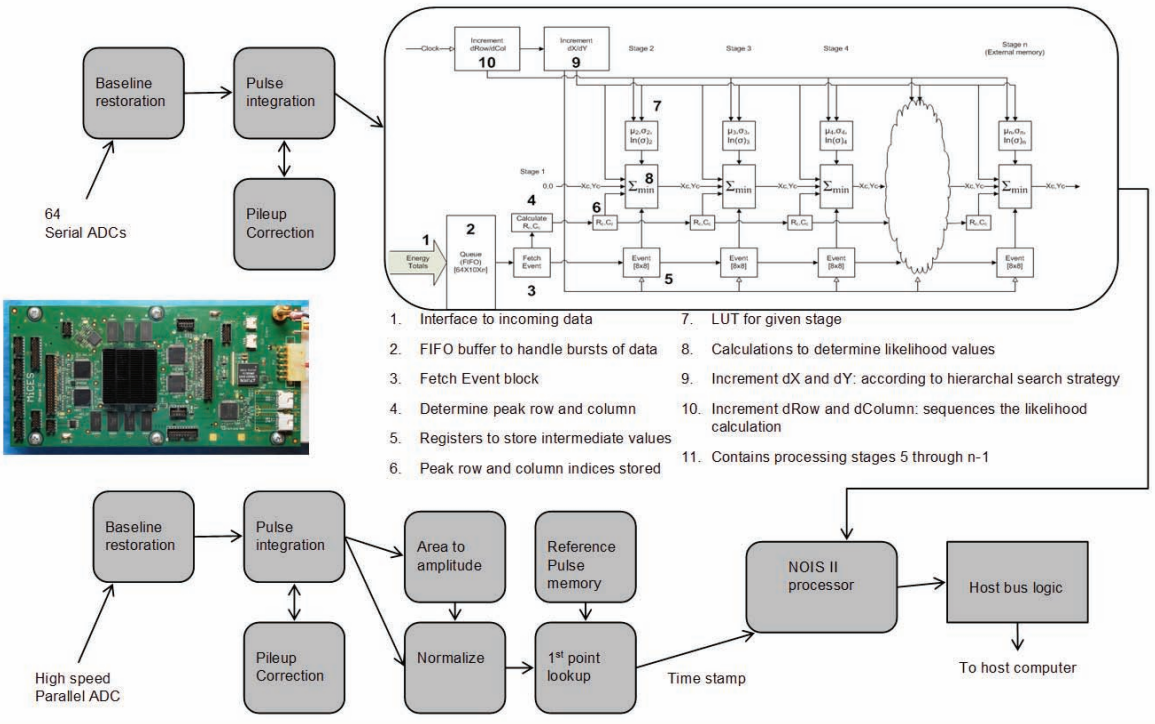

1. Interface to incoming data
2. FIFO buffer to handle bursts of data
3. Fetch Event block
4. Determine peak row and column
5. Registers to store intermediate values
6. Peak row and column indices stored
7. LUT for given stage
8. Calculations to determine likelihood values
9. Increment dX and dY: according to hierarchal search strategy
10. Increment dRow and dColumn: sequences the likelihood calculation
11. Contains processing stages 5 through n-1

Ultimate time resolution in TOF PET scanners

Paul Lecoq
CERN, Geneva, Switzerland

The future generation of radiation detectors is more and more demanding on timing performance for a wide range of applications, such as time of flight (TOF) techniques for PET cameras and particle identification in nuclear physics and high energy physics detectors, precise event time tagging in high luminosity accelerators and a number of photonic applications based on single photon detection.

The time resolution of a scintillator-based detector is directly driven by the density of photoelectrons generated in the photodetector at the detection threshold. At the scintillator level it is related to the intrinsic light yield, the pulse shape (rise time and decay time) and the light transport from the gamma-ray conversion point to the photodetector. When aiming at 10ps time resolution fluctuations in the thermalization and relaxation time of hot electrons and holes generated by the interaction of ionization radiation with the crystal become important. These processes last for up to a few tens of ps and are followed by a complex trapping-detrapping process, Poole-Frenkel effect, Auger ionization of traps and electron-hole recombination, which can last for a few ns with very large fluctuations.

This talk will review the different processes at work and evaluate if some of the transient phenomena taking place during the fast thermalization phase can be exploited to extract a time tag with a precision in the few ps range.

The light transport in the crystal is also an important source of time jitter. In particular light bouncing within the scintillator must be reduced as much as possible as it spreads the arrival time of photons on the photodetector and strongly reduces the light output by increasing the effect of light absorption within the crystal. It concerns typically about 70% of the photons generated in currently used scintillators.

A possible solution to overcome these problems is to improve the light extraction efficiency at the first hit of the photons on the crystal/photodetector coupling face by means of photonic crystals (PhCs) specifically designed to couple light propagation modes inside and outside the crystal at the limit of the total reflection angle.

Why fast timing in PET scanners?

- TOF for rejecting backround events (event collimation)
  - Requires 200ps TOF resolution
- TOF for improving image S/N
  - 100ps TOF resolution improves S/N by a factor of ≈ 5
- TOF for direct 3D information
  - Requires 1 to 2mm resolution along LOR ➔ 10ps TOF resolution

Factors influencing scintillator time resolution

P. Lecoq et al, IEEE Trans. Nucl. Sci. 57 (2010) 2411-2416

Besides all factors related to photodetection and readout electronics the scintillator contributes to the time resolution through:

1. The scintillation mechanism
   - Light yield,
   - Rise time,
   - Decay time
2. The light transport in the crystal
   - Time spread related to different light propagation modes
3. The light extraction efficiency (LY➔LO)
   - Impact on photostatistics
   - Weights the distribution of light propagation modes

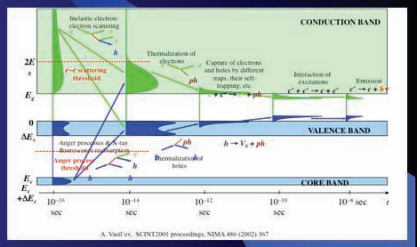

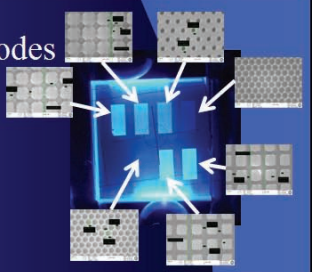

The Development and Applications of a small animal simultaneous SPECT/MR imaging system

B. M. W. Tsui[1], J. Xu[2], A. Rittenbach[2], A. M. El-Sharkawsay[2], W. A. Edelstein[2], K. ParnHam[3] and J. W. Hugg[3]

[1] Department of Radiology, Johns Hopkins University, U.S.A., btsui1@jhmi.edu, [2] Department of Radiology, Johns Hopkins University, U.S. A., [3] TriFoiling Imaging, U.S.A.

This paper presents the development and applications of a SPECT/MR insert for simultaneous SPECT/MR imaging of small animals. A second generation SPECT/MR insert was developed based on a first generation insert demonstrating the feasibility of simultaneous SPECT/MR. It consists of 5 rings of 19 seamlessly connected 2.54x2.54 cm^2, 16x16 pixels cadmium zinc telluride (CZT) detectors. The CZT detectors directly convert incident photons into electric signals and hence are minimally affected by the static magnetic field of the MRI. Two multi-pinhole (MPH) collimators of 18 and 36 PHs were designed with 1.0 and 1.5 mm resolution, respectively. The collimators were made of a cylindrical shell filled with high density tungsten powder and solid tungsten pinhole inserts. A shielded birdcage quadrature transmit/receive RF coil was designed for mouse imaging. It fit inside the MPH collimator to maximize SNR. Accurate system calibration and quantitative sparse-view 3D MPH reconstruction methods were developed for high quality SPECT images.

The measured resolutions of the both collimators agreed with their targeted system resolutions and measured detection efficiencies were 172 and 372 cps/MBq, respectively. The predicted Lorenz force effect on the CZT detectors was observed and corrected. With collimator-detector response modeling, the SPECT image resolution exceeded the target system resolution of the MPH collimators. Artifact-free high quality MPH SPECT images were obtained from experimental phantom studies using a Data Spectrum hot spot phantom and from small animal MPH SPECT studies using the SPECT subsystem. Placing the SPECT-MRI insert inside a 3T clinical MRI system, we demonstrated its feasibility for simultaneously SPECT-MR imaging study in experimental phantom studies. The simultaneously acquired SPECT, MR and the registered fused SPECT-MR images were in good agreement.

We performed a simultaneous dynamic SPECT-MRI kidney function study, a 30 min data acquisition in listmode format was initiated with a tail vein injection of ~2.5 mCi of ^{99m}Tc-MAG3. The listmode data were rebinned into 10-sec time frames before image reconstruction into 180 dynamic SPECT images showing the uptake and washout of ^{99m}Tc-MAG3 by the kidneys. Five 1-mm thick with 0.75 mm spacing coronal slices were acquired dynamically in 80 sec time frames for ~30 minutes using a multi-slice fast field echo (FFE) pulse sequence simultaneously with the SPECT data acquisition. The combined 30 min SPECT, MR and the fused SPECT-MR images again showed minimum artifacts and distortions.

The results demonstrated the ability of the second generation SPECT/MR insert to obtain high quality small animal whole body dynamic studies and the feasibility of simultaneous small animal SPECT-MR imaging. Other applications for the SPECT/MR system are being explored.

Rationale and Completed SPECT/MR Insert

- Rationale
  - Novel technique: *for **simultaneous** multi-modality molecular Imaging*
  - MRI: *provides anatomical & functional information without radiation*
  - SPECT: *allows multiple functional information w/ different radioitracers*
- Challenges that have been overcome
  - Effect of magnetic field B_o on SPECT: *avoided using solid-state CZT detectors*
  - Effects of B_o on electron transport (Lorentz force) in CZT detectors: *corrected*
  - Effects of SPECT on MRI: *avoided using special collimator materials & design*
  - High SPECT resolution & sensitivity: *achieved using multi-pinhole (MPH) collimator*
  - High S/N MR images: *achieved using specially designed RF coils*
- A completed SPECT/MR insert

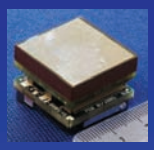

MR compatible CZT detector module w/ 2.54x2.54cm² 16x16 pixels

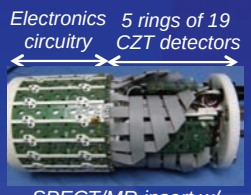

SPECT/MR insert w/ cover off

SPECT/MR insert & w/ cover

Specially designed & fabricated MPH collimator

Birdcage T/C coil inside the MPH collimator

Placement of the SPECT/M… inside a P… clinical MR… canner

Sample Results

Stand-alone SPECT Acquisition

Phantom Study

Data Spectrum Ultra-Micro phantom

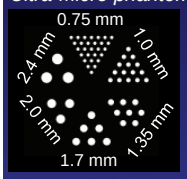

18-Pinhole resolution: 1.0mm

36-Pinhole resolution: 1.5 mm

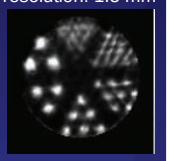

^{99m}Tc-MDP study of a mouse's head*

18-Pinhole resolution: 1.0 mm

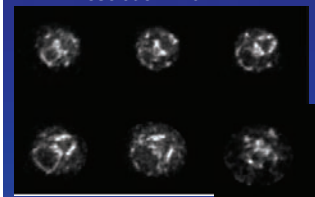

36-Pinhole resolution: 1.5 mm

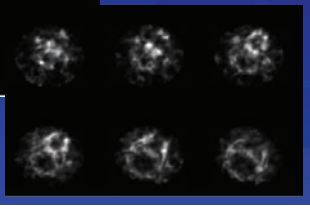

** 3D MPH ML-EM with 40 iteration w/ CDRF correction & post smoothing*

Simultaneous SPECT/MR Acquisition

Phantom Study

SPECT

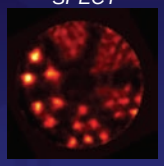

MR

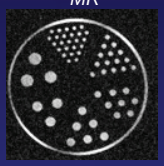

Fused SPECT/MR

Dynamic ^{99m}Tc-MAG3 mouse kidney study

10 sec/frame dynamic SPECT

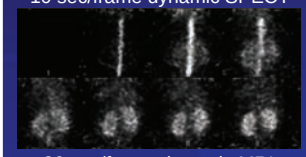

30 min summed SPECT

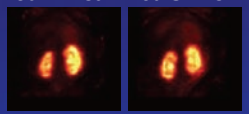

80 sec/frame dynamic MRI

30 min summed MRI

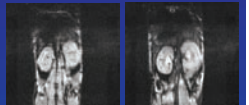

TAC of kidneys in 10 sec/frame

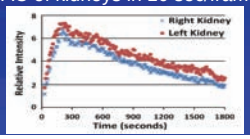

30 min fused SPECT/MRI

Medical application of radioisotope beams and trials at HIMAC

Atsushi Kitagawa[1], Yoshiya Furusawa[1], Masahito Hosaka[4], Yasushi Iseki[2], Tatsuaki Kanai[5], Mitsutaka Kanazawa[6], Shigeru Koda[7], Qiang Li[3], Hideyuki Mizuno[1], Takeshi Murakami[1], Masayuki Muramatsu[1], Teiji Nishio[8], Koji Noda[1], Shinji Sato[1], Mitsuru Suda[1], Takehiro Tomitani[1], Eriko Urakabe Shintani[1], Satoru Yamada[1], Kyosan Yoshikawa[1]

[1] NIRS, Japan, kitagawa@nirs.go.jp, [2] Toshiba co., Japan, [3] IMP, China (Present address: [4] Nagoya Univ., Japan, [5] Gunma Univ., Japan, [6] Saga HIMAT, Japan, [7] Saga Univ., Japan, [8] National Cancer Center, Japan)

A short-lived positron emitting nuclei, such as ^{11}C, ^{15}O or ^{19}Ne, gives a localized distribution of positrons and it is available to determine its position by detecting a pair of gamma-rays. This phenomenon makes ideas to precisely determine a region in human body irradiated by charged particles since 1970's. An incident proton beam was produced various positron emitting nucleus, such as ^{15}O, ^{13}N, and ^{11}C, from human tissues by the target fragmentation and was utilized to detect by a Positron Emission Tomography (PET) system[1]. Since a part of incident ^{12}C beam changes to ^{11}C by the projectile fragmentation, these ^{11}C, so-called 'autoactivation', were also available[2,3]. However, these measurements have ambiguities due to the reaction.

Alternatively, a direct use of radioisotope beam (RIB) gives a large advantage. Its signal-to-noise ratio is higher than the autoactivation's and the relation between the measured distribution and the actual stopping position of the beam is clear. The medical application of the RIB was originally studied at BEVALAC of the Lawrence Berkeley Laboratory[4]. Although their early results showed useful data, unfortunately, BEVALAC was shut down before the full completion of the RIB application.

In order to study such a medical application for heavy ion radiotherapy, the secondary beam course (SBC) at the Heavy Ion Medical Accelerator in Chiba (HIMAC) of National Institute of Radiological Sciences (NIRS) has been developed since 1994. In order to obtain RIB, the projectile fragmentation method is used. Projectile particles of a primary beam produce various fragment particles through nuclear reaction mechanism in a target. The fragment particles since have the same velocity and the same angular distribution which concentrate to forward direction, it is available to use as the secondary beam. The on-line isotope separator which identify and separate the required isotope from various fragments is comprised of two dipole magnets. One is the fragment momentum analyzer by the rigidity analysis, the particles which have same charge-to-mass ratio are selected. These same A/Z fragments are decreased their energy by the thick energy-degrader. The energy losses are due to their charge. The other analyzer after the energy degrader separates the only required particles by these new rigidities. The particle is identified by the beam monitor measured its energy loss and time of flight.

Figure 1 shows a schematic view of SBC. There are two experimental ports, SB1 and SB2. SB1 has a beam irradiation system and is able to produce ^{11}C with an energy of 350MeV/u and a typical production rate of $2x10^{-4}$with the momentum spread of 0.4%. The maximum 3-D irradiation volume is 10x10x18 cm with a pencil beam spot scanning. Details of the secondary beam course for the production of RNB and the beam irradiation system have been reported in references [5,6]. SB2 has no irradiation system and is utilized for various fundamental experiments.

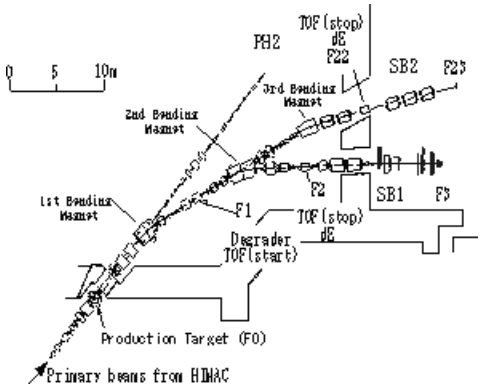

Figure 1.A schematic view of SBC at HIMAC.

For the detection of the precise depth location with the least dose given to a patient, we developed the Positron Camera detector[7]. The experimental results with phantoms showed a good instrumental accuracy of 0.6mm with the biological dose of 0.1 GyE (3 x 105 particles). More developments of the PET detector system has been continued by PET group energetically[8].

We measured the lifetimes of the ^{10}C and ^{11}C in the alive and dead rabbits' brains and muscles. The lifetime in the alive rabbit has at least three components. These components are due to the very fast blood-stream in the blood vessel, the regional blood flow in the muscle tissue, and unknown products which had the slow diffusion speed. These results suggest the importance of the biological and chemical process in the metabolism for clinical use.

References

[1] G.W. Bennett et al., Science 200, 1151 (1978).
[2] C.A. Tobias et al., Int. J. Radiat. Oncol. Biol. Phys. 3, 35 (1977).
[3] K. Yoshikawa et al., J. Nucl. Med. Technol. 24, 167 (1996).
[4] C.A. Tobias et al., Int. J. Radiat. Oncol. Biol. Phys. 3, 35 (1977).
[5] M. Kanazawa et al., Nucl. Phys. A 701, 244 (2002).
[6] E. Urakabe et al., Jpn. J. Appl. Phys. 40, 2540 (2001)
[7] Y. Iseki et al.,Phys. Med. Biol. 49 (2004) 1.
[8] E. Yoshida et al. in this workshop.
[9] H. Mizuno et al., Phys. Med. Biol. 48 (2003) 2269.

Medical application of radioisotope beams (RIB)

NIRS HIMAC

Principle of the measurement

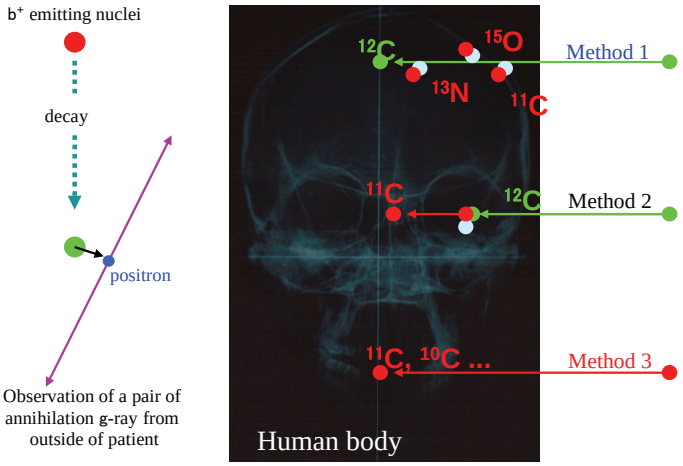

Methods of production for b+

1. In-vivo activation method:
   Stable beam produces b+-emitter as target fragment.
2. Autoactivation method:
   Stable beam changes to b+-emitter as projectile fragment.
3. Radioactive nuclear beam method:
   directly shows it's position with high signal-to-noise ratio.

Production method of RIB

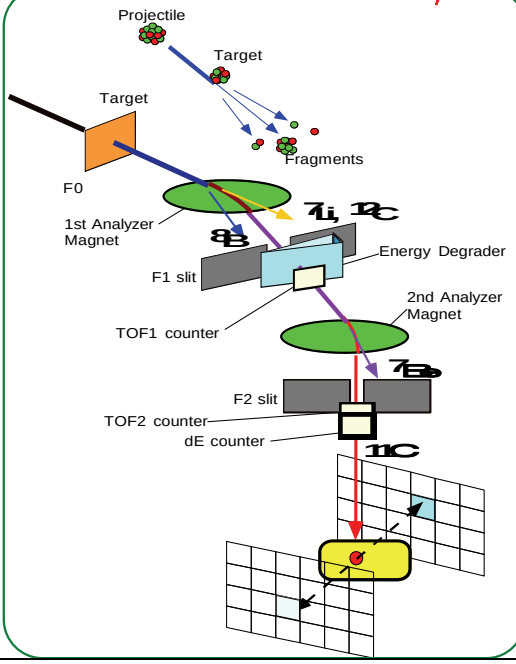

Trials at HIMAC

NIRS HIMAC

1-D range information in the PMMA phantom

Beam condition

^{10}C & ^{11}C beam energy :	346 MeV/u (range=156.9mm in PMMA)
Momentum width :	0.8% (FW) (Drange=3.6mm)
Beam size :	7 mm (FWHM)
Intensity :	300-500k pps (110-180mGy)

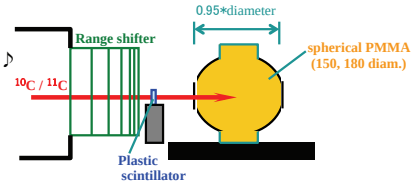

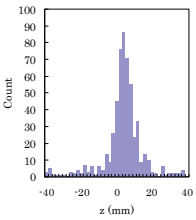

Accuracy of the centroid of the stopping point in the phantom = 0.6 mm

Metabolism study by rabbits

Beam condition

^{10}C & ^{11}C beam energy :	346 MeV/u
Momentum width :	0.4% (FW)
Beam size :	3 - 7 mm (FWHM)
Intensity :	24k (^{10}C) pps
	300k (^{11}C)

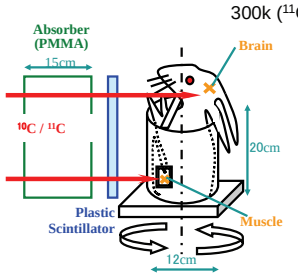

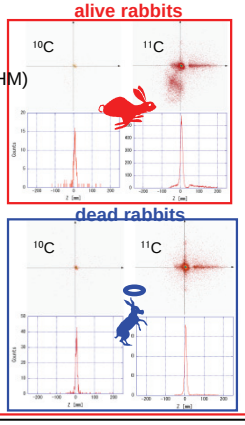

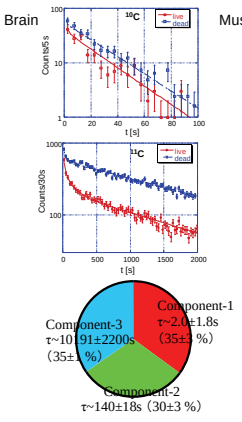

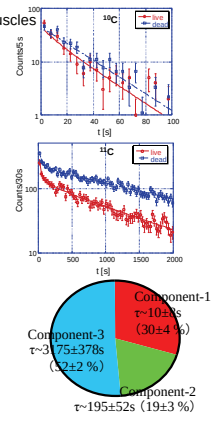

3-components Biological model of wash out

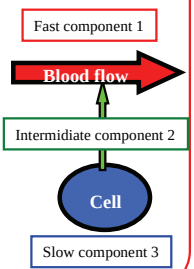

Offline PET-based Treatment Verification at the Heidelberg Ion-Beam Therapy Center: Clinical Experience and On-Going Research

Christopher Kurz[1], Julia Bauer[1], Daniel Unholtz[1], Kathrin Frey[2], Chiara Gianoli[1], Guido Baroni[3], Stephanie Combs[1], Jürgen Debus[1] and Katia Parodi[1,2]

[1] Heidelberg Ion-Beam Therapy Center and Department of Radiation Oncology, Heidelberg University Hospital, Heidelberg, Germany, christopher.kurz@med.uni-heidelberg.de

[2] Department of Experimental Physics – Medical Physics, Ludwig-Maximilian-University, Munich, Germany

[3] Department of Electronics Information and Bioengineering, Politecnico di Milano, Milano, Italy

At the Heidelberg Ion-Beam Therapy Center (HIT), the activation of patients during the irradiation with protons or carbon ions is used to verify the correct application of the planned treatment. For this purpose, the induced activity within the patient is measured by a commercial full-ring PET/CT scanner installed next to the treatment rooms (offline) and compared to a Monte-Carlo (MC) simulation based on the patient-specific treatment plan, taking the time-course of the irradiation and the biological wash-out of the created isotopes into account.

In more than 100 investigated patient cases with tumors at various locations within the body, the method proved to be particularly suitable for the monitoring of irradiations in the head and neck region. Similar to the findings in [1,2] for passively scattered proton therapy, a generally good agreement between MC prediction and actual PET measurement was observed and a reliable analysis of the beams range was possible (see figure 1). Further improvements are however still foreseen by the currently studied Magnet-Resonance-Imaging (MRI) based segmentation of white and grey matter within the brain, which show significant differences in their carbon abundances, resulting in a different amount of the irradiation induced β^+ emitter ^{11}C.

Valuable clinical results could, among others, also be achieved in the monitoring of sacral Chordoma irradiations, which are particularly sensitive to changes in the patient anatomy, e.g., due to weight-loss, and patient positioning [3].

One main challenge of offline PET-based treatment verification was found in the low amount of irradiation-induced activity, being orders of magnitude lower than in typical nuclear medicine applications, for which commercial PET/CT scanners are optimized. As a consequence, the acquired images suffer from remarkable noise and a thorough interpretation of the acquired data can be hindered in some cases. However, it was found that the choice of a proper reconstruction algorithm and its optimal parameters, typically differing from those used in nuclear medicine, could significantly reduce the image noise without a loss of accuracy in quantification and geometrical resolution [4]. In addition, more sophisticated techniques of analyzing the acquired PET data in beam's eye view are currently under investigation and promise to result in a more reliable range verification by in-vivo PET imaging.

Still, the low counting statistics is a particularly crucial point if the irradiated area is affected by organ motion and a time-resolved (4D) analysis of the acquired data is desirable. While the feasibility of 4D therapy monitoring has already been demonstrated in first simplified moving phantom experiments [4], application to clinical cases is at present limited by the low number of true coincidences in combination with the currently used 4D gated PET image reconstruction. Improvements by a more noise-robust reconstruction algorithm are another subject of current investigation.

In this contribution, typical patient cases for post-irradiation verification by means of offline PET/CT-imaging will be discussed, and an overview of the on-going research activities at HIT will be given.

Acknowledgements: This work has been supported by the FP7 EU project ENVISION

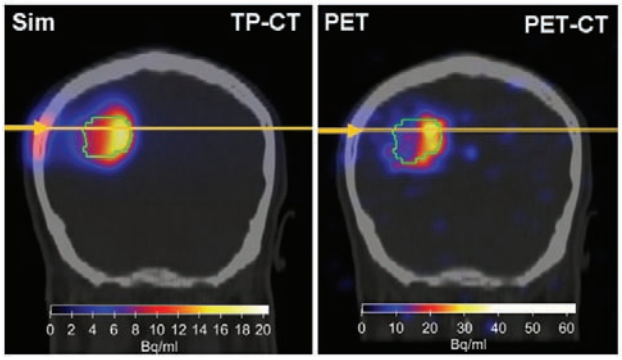

Figure 1: *Comparison of post-irradiation PET/CT measurement (right) and MC prediction (left), corrected for irradiation time-course and biological wash-out, in a Glioblastoma patient. The beam was entering along the depicted yellow arrow. The green line marks the planning target volume (PTV). A good agreement between measurement and prediction concerning the shape of the activity and the beam range was found. Quantitatively, the measured activity is found to be in good agreement within the cranial bone, but significantly higher in the PTV, probably due to limitations of the wash-out modeling in the simulated data.*

References

[1] Parodi et al, *Int J Radiat Oncol Biol Phys*, **2007**
[2] Knopf et al, *Phys Med Biol* 54(14), **2009**
[3] J Bauer et al, *Radiother Oncol* 107, **2013**
[4] C Kurz et al, *IEEE MIC*, **2013**, submitted

Offline PET-based treatment verification at the Heidelberg Ion-Beam Therapy Center

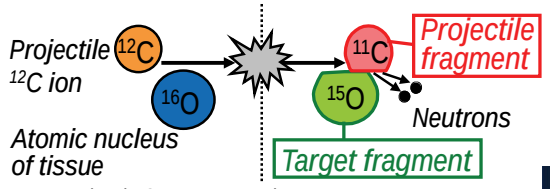

W. Enghardt, OncoRay Dresden

- **β⁺ emitter** formed as **by-product** of the **irradiation** in **nuclear fragmentation** reactions

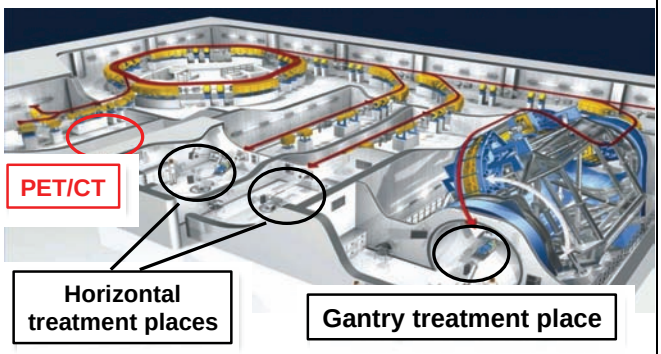

- Induced β⁺ **activity detected** in-situ and non-invasively with **commercial PET/CT** scanner installed **next to the treatment site** (offline)

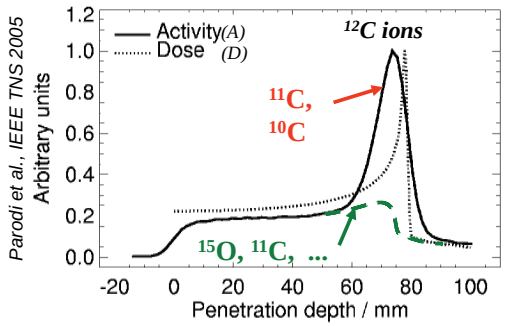

- As $A(r) \neq D(r)$ the **measured activity** needs to be **compared to** an **expectation** calculated on the **basis of the treatment plan** in the verification process

Offline PET-based treatment verification at the Heidelberg Ion-Beam Therapy Center

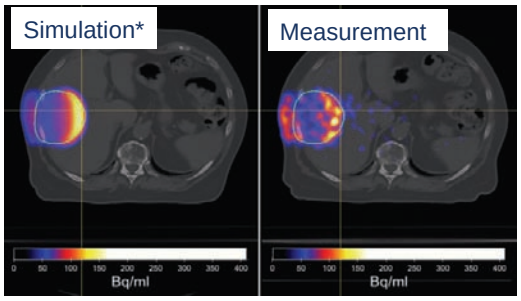

* plus post-processing

- **Clear correlation** between **simulation** and **measurement** was observed in the **head and neck** region, for **hepato-cellular carcinoma** (see left fig.) and **sacral chordoma patients** (see fig. below)
- In particular, **valuable information** on the **beam range** could be retrieved

- In the depicted sacral chordoma case, (clinically uncritical) **range deviations** due **patient mis-positioning** could be **detected** and cor-rected for in the next session
- The **main limiting factor** in **offline PET-based treatment verification** was found to be the **low** amount of **induced activity**, leading to **remarkable noise** in the PET images

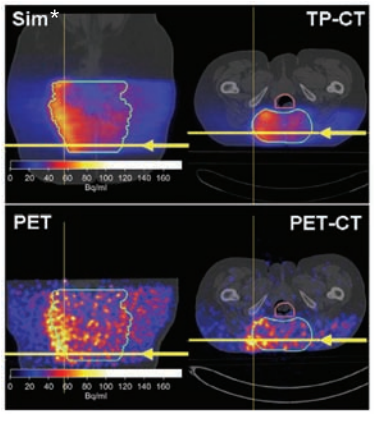

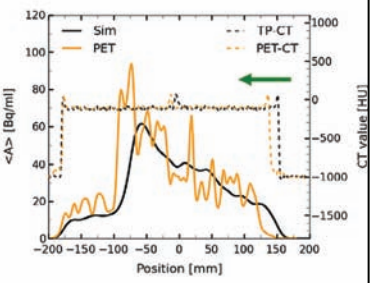

J. Bauer et al, Radiother Oncol 2013

Development of data acquisition system for the human OpenPET

Eiji Yoshida[1], Keiji Shimizu[2], Taiga Yamaya[1]

[1] National Institute of Radiological Sciences, Japan, rush@nirs.go.jp, [2] Hamamatsu Photonics K.K., Japan

1. Introduction

One of the challenging applications of PET is implementing it for in-beam PET, which is an *in situ* monitoring method for charged particle therapy. For this purpose, we have previously proposed two geometries for our open-type PET scanners named OpenPET. Also, we developed three small prototypes and promises good potential for in-beam. On the other hand, for in-beam PET, careful designing and testing of detectors are important because secondary particles generated in a target degrade detector performance in the OpenPET geometry [1] and the quantity of positron emitters produced in in-beam PET is very small. We are developing the human size OpenPET. In this work, we developed data acquisition (DAQ) system for the human OpenPET.

2. Material and methods

Figure 1 shows the DAQ system prototype for the human OpenPET. This DAQ system had no coincidence circuit and only single list-mode data acquisition system. Obtained single data judgment to coincidence based on software, where the single list-mode data include 6 bits energy and 500 ps timing information. The depth-of-interaction (DOI) detector consisted of 1024 GSOZ crystals which were arranged in 4 layers of 16 × 16 arrays and coupled to the position sensitive photomultiplier, connected to this DAQ system.

Irradiation tests were done at HIMAC using the developed DAQ system. The energy and intensities of the ^{12}C beam were 290 MeV/u and 10^5 – 10^8 particles per second (pps), respectively. The DOI detector was positioned 30 cm from the backside of the water phantom at an angle of 30 deg. Beam-spill interval of HIMAC was 3.3 s. (Spill on was irradiation of 1.9 s and spill off was pause of 1.4 s.) In spill on, most data are noise events based on secondary particles and prompt gamma rays. The DAQ system can extract data of spill off using the timing information.

3. Results

Figure 2 shows 2D position histograms in spill on and spill off for several beam intensities. The ^{22}Na point source was positioned at the front of the detector for evaluating 2D position histogram. Over 10^7 pps irradiation, 2D position histograms in spill on had an artifact and shrunk. On the other hand, 2D position histograms in spill off obtained sufficient crystal identification performance around 10^8 pps, although the 2D position histogram was degrading slightly with increasing ^{12}C beam intensity.

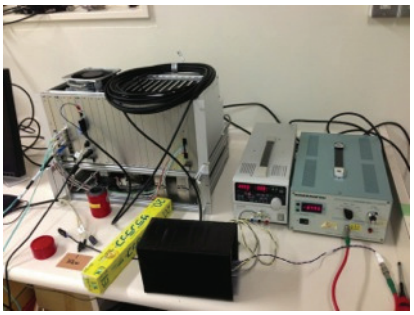

Figure 1. DAQ system prototype for the human OpenPET.

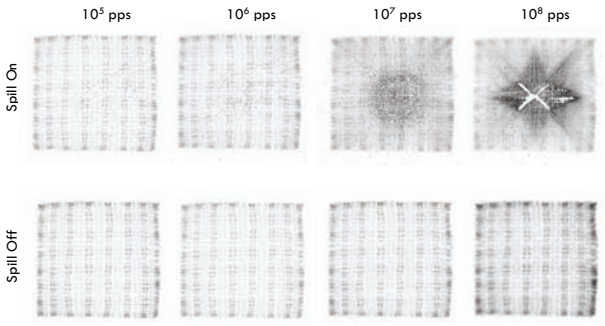

Figure 2. 2D position histograms in spill on and spill off for several beam intensities.

4. Conclusions

We developed the DAQ system for the human OpenPET. This DAQ system promises sufficient crystal identification performance around 10^8 pps.

References

[1] F.Nishikido, Y.Hirano, N.Inadama, et al., "Optimization of the in-beam OpenPET detector for carbon beam irradiation" *NSS-MIC 2012*, M22-2. 2012.

OpenPET

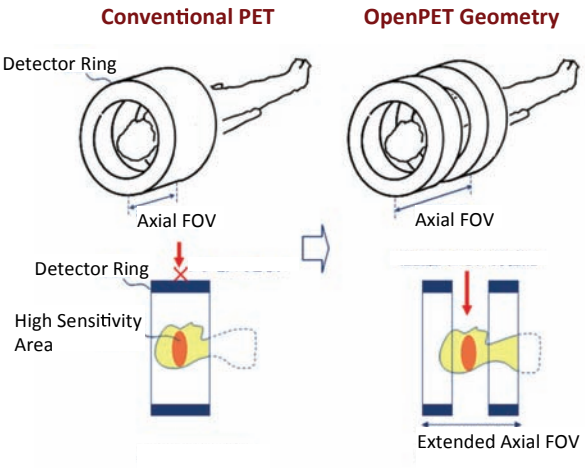

(a) Dual-ring OpenPET (First generation)

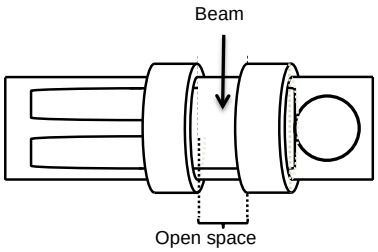

(b) Single-ring OpenPET (Second generation)

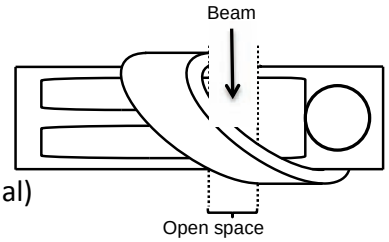

OpenPET
- Extend axial FOV (entire body PET)
- Applications using open space (in-beam PET, multimodal)

Single ring OpenPET
- Can focus sensitivity to open space in comparison with dual ring OpenPET.

One-pair prototype DAQ system

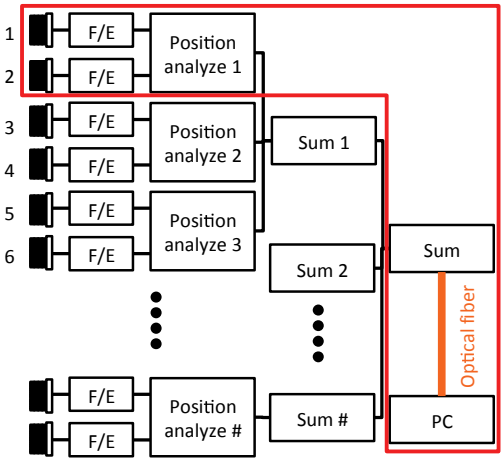

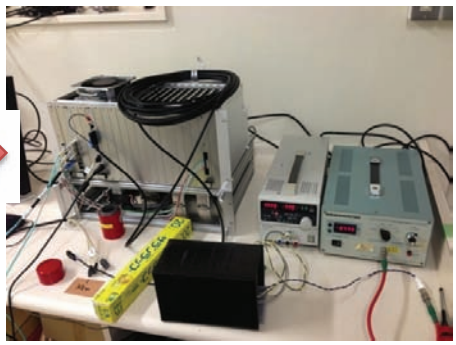

Detector flood image (^{22}Na source)

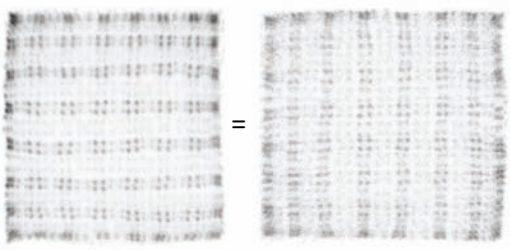

Off-site = In-beam (off spill) 10^7 pps

- Single data acquisition (software coincidence)
  - For intelligent data analysis
- High throughput
  - ~30Mcps
- High stability of detector response at high intensity beam

Time-of-Flight PET in clinical and application-specific imaging

Suleman Surti[1]

[1] Dept. of Radiology, University of Pennsylvania, USA, surti@mail.med.upenn.edu

Time-of-Flight (TOF) PET imaging was originally developed in the 1980s and used primarily for brain and cardiac imaging. In recent years TOF PET has been re-introduced clinically while making use of new scintillators to collect data in a fully-3D mode and reconstructing images with iterative 3D reconstruction algorithms. Past studies have shown that TOF PET improves image signal-to-noise ratio (SNR) that is proportional to the square root of the object size and inversely proportional to the square root of the system timing resolution can be achieved[1,2]. However these results were obtained with analytical reconstruction algorithms and data acquired in 2D mode with septa present in scanner FOV.

In recent years, PET has been primarily used in oncology where lesion detection and quantification are the main tasks performed by the clinicians. Simulations as well as measurements show a faster and more uniform convergence of lesion contrast in physical phantoms[3-8]. Consequently improved trade-offs between contrast, noise, and scan time are obtained that lead to improved lesion detection and uptake estimation with TOF PET. Lesion detectability studies using numerical or human observers show improved performance in uniform objects and anthropomorphic phantoms with improving timing resolution[3,9-10].

We have performed a clinically realistic study where artificial lesions (plastic spheres) were added to healthy patient data in list-mode followed by image reconstruction. A human observer study was then performed to calculate the LROC curves and the corresponding area under the LROC (ALROC) metric. Results showed that with TOF imaging there was a bigger increase in the area under the LROC curve for larger patients (BMI $\geq$ 26). Combining longer scan times with TOF imaging we saw smaller differences in the ALROC values for large and small patients, indicating a more uniform clinical performance over all patient sizes. In a related study we used this technique of adding lesions artificially to patient data to quantify the impact of TOF PET on the accuracy and precision of lesion uptake measurements. Our results show an increase in average uptake over all spheres and patients with TOF compared with Non-TOF reconstruction at comparable noise levels. The variability in the uptake measurement across replicates, over spheres within an organ, and across all spheres and subjects is also reduced with TOF compared to Non-TOF reconstruction. Summary results from both the lesion detection and uptake estimation studies will be presented.

Beyond clinical studies, it has also been observed that TOF image reconstruction is less sensitive to inconsistencies between emission data and corrections such as attenuation, normalization, and scatter [11]. In addition, TOF information was shown to be beneficial in reconstructing images when limited angular views of the object are available due to a partial scanner ring. We utilize this advantage in two application-specific imaging scenarios (*in-situ* PET for proton beam range verification and dedicated breast PET imaging) where a partial scanner ring provides the flexibility needed for patient imaging.

PET scanners for proton beam range verification require high sensitivity, plus the ability to record data straight after irradiation while the patient is still on the treatment bed. The latter feature is essential to maximize positron detection, particularly from short-lived isotopes that may decay during patient transfer to a separate scanner. Such *in-situ* scanning requires the use of a partial detector ring, to meet patient positioning restrictions and avoid interference between PET detectors and the proton beam. Design optimization studies were performed as a function of system timing resolution and scanner angular coverage. For a full-ring, non-TOF scanner we predict a low bias (< 0.6-mm) and a good precision (< 1-mm) in the estimated range relative to the simulated positron distribution. We then varied the angular acceptance of the scanner ranging from 1/2 to 2/3 of 2π; with a partial ring TOF imaging with good timing resolution ($\leq$ 600ps) is necessary to produce accurate tomographic images. Our results indicate that it would be feasible to develop a partial-ring dedicated PET scanner based on either $LaBr_3$ or LYSO to accurately characterize the proton dose for therapy planning. Ongoing work involves development of a two detector module using $4x4x30mm^3$ $LaBr_3$ crystals to demonstrate the feasibility of this system. Results from the simulation studies as well as the system development will be presented.

Monitoring primary tumor response to neo-adjuvant therapy in breast cancer is a promising area of research where a high spatial resolution breast PET scanner can play an important role. We are utilizing the benefit of achieving good lesion uptake measurement in a partial ring TOF breast scanner to develop a high spatial resolution dedicated breast PET scanner. Simulation studies indicate the capability to achieve good quantitation in two-third angular coverage system with timing resolution of 600ps or better. We have developed a PET detector using $1.5x1.5x15mm^3$ LYSO crystal coupled to a multi-anode PMT to achieve good crystal separation as well as excellent energy (13% at 511 keV) and timing resolution (350ps). Simulation and preliminary experimental imaging results from this system will be presented.

In conclusion, this presentation will summarize results from the impact of TOF PET in clinical diagnostic work as well as demonstrate its potential for use in proton beam range verification and dedicated breast imaging.

References

1. Budinger TF: J. Nucl. Med. 24:73-76, 1983.
2. Tomitani T:.IEEE Trans. Nucl. Sci. 28:4582-4589, 1981.
3. Surti S, et al: IEEE Trans. Med. Imag. 25:529-538, 2006.
4. Conti M, et al: Phys. Med. Biol. 50:4507-4526, 2005.
5. Vandenberghe S, et al: J Nucl Med 47:58P, 2006.
6. Surti S, et al: J. Nucl. Med. 48:471-480, 2007.
7. Karp JS, et al: J. Nucl. Med. 49:462-470, 2008.
8. Lois C, et al: J. Nucl. Med. 51:237-245, 2010.
9. Surti S, Karp JS: Phys. Med. Biol. 54:373-384, 2009.
10. Kadrmas DJ, et al: J. Nucl. Med. 50:1315-1323, 2009.
11. Conti M: Phys. Med. Biol. 56:155-168, 2011.

TOF PET in clinical ^{18}F-FDG imaging

Method: Spherical lesion data added to healthy patient list-mode data followed by image reconstruction

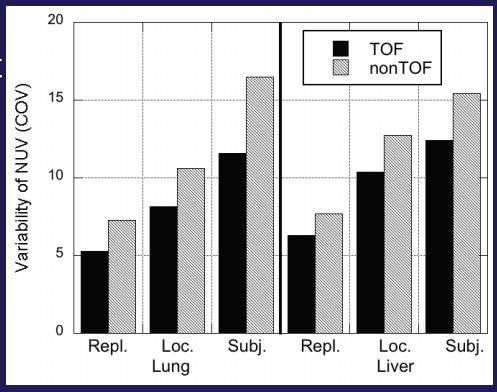

Result 1: Variability in lesion uptake measurement is reduced with TOF over: (i) multiple replicates, (ii) lesion location, and (iii) multiple patients

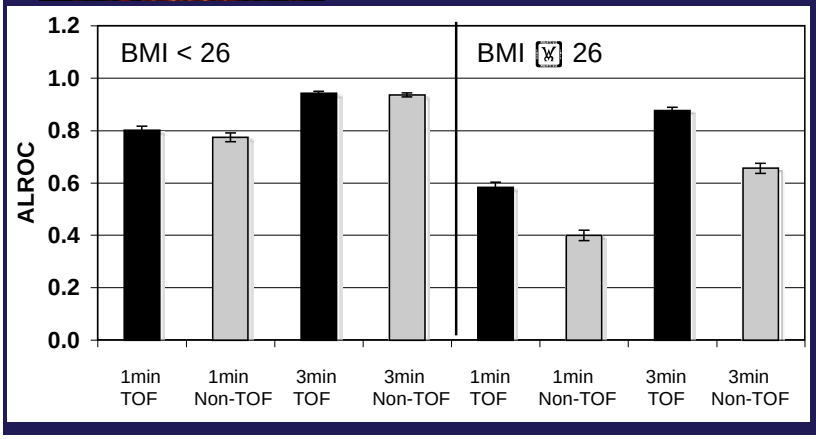

Result 2:

Human observer study for lesion detection and localization shows that: (i) ALROC is higher with TOF esp. in larger patients, (ii) longer (3 mins) scan time together with TOF imaging leads to more uniform ALROC over different patient sizes and organ

In-situ dose verification of proton dose

System Design simulations: 30-cm diameter cylinder irradiated by 4x4-cm^2 125-MeV proton beam, b^+ profile from GEANT4 simulation in skeleton muscle, PET simulations performed in EGS4

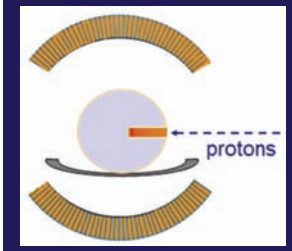

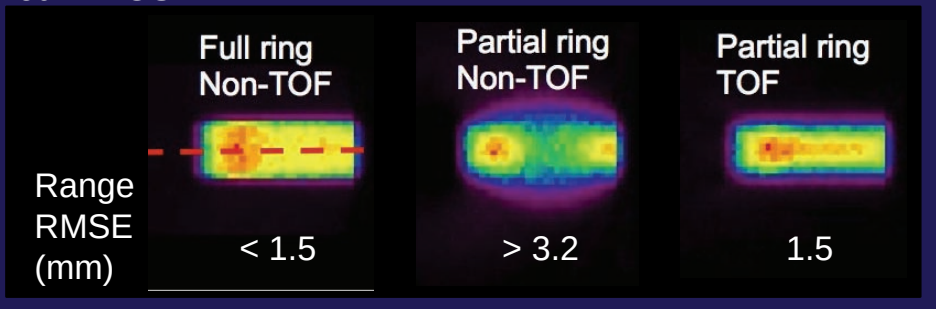

Prototype system development

$LaBr_3$ detector modules
Intrinsic timing resolution ~ 300-350ps

Coincidence detector setup
NIM/CAMAC electronics

Evaluation of open-ring imaging systems for range verification in proton-therapy by means of secondary radiation

I. Torres-Espallardo[1], J. E. Gillam[1], P. Solevi[1], P. G. Ortega[2], P. Botas[1], J. F. Oliver[1], G. Llosá[1], M. Trovato[1], C. Solaz[1], C. Lacasta[1] and M. Rafecas[1]

[1] IFIC (Univ. Valencia/CSIC), Spain, irene.torres@ific.uv.es, [2] CERN, Switzerland

Total patient dose reduction and energy dependence on the finite range of the proton are the main advantages of the protontherapy. The latter increases flexibility during treatment planning, providing an additional variable, improving target conformality. But also, proton range is associated with several uncertainties that must be addressed in order to obtain a successful outcome: therefore range verification is necessary to treatment optimization and patient safety. Given that the primary protons do not exit the patient, standard portal imaging cannot be used for QA. Thus, the monitoring method can only be based on secondary emerging radiation, such annihilation photons [1] and prompt gamma radiation [2]. Secondary particles are considered because there is a relation, though not direct, between both the range and deposited energy of the proton beam and the production of secondary photons along the beam path. The annihilation photons are the consequence of a positron emitter distribution, generated by proton induced nuclear interactions. The detection of annihilation photons by means of PET is used clinically for range verification, but it has some limitations using standard scanners, like the low positron yield and the biological wash-out processes. To reduce the effect of wash-out and in order to measure short half-life positron emitters, in-beam PET has been proposed which requires an opening in the radius of the scanner. An open-ring geometry produces some artifacts in the reconstructed image that could be compensated for by the use of time-of-flight (TOF) information. Prompt gamma are highly energetic photons emitted in a very short period after the proton passage, less than 1 ns, and arise from excited nuclear states induced by proton-nucleus interactions. Their detection using Compton Cameras (CCs) is a promising verification technique [3] and offers the possibility of real-time monitoring, although it has not been used clinically. The goal of this work is to study the ability of the open ring PET geometries with TOF and of the proposed Compton Camera for assessing range shifts below 5 mm. All this work is part of the ENVISION project which is directed towards on-line dose monitoring in hadrontherapy.

In order to evaluate the capability to reproduce the distal edge of the proton beam, a set of sources emulating the annihilation photons from β+-emitters produced after proton pencil beam irradiation (5×10^7 protons) on a PMMA target (75 mm radius and 200 mm length) was simulated in Geant4.9.3. The energy of the proton beam was varied from 158 to 162 MeV in 3 steps to produce a 3 mm range shift in each. The geometries of the PET scanner are a C-shape (C-PET) and a standard partial ring with two apertures (PR-PET). The diameter is varied from 60 to 40 cm to increase sensitivity. The detectors heads are 30° continuous sectors of 2.2 cm deep and 30 cm axial extension. In the simulations we have included a realistic coincidence time resolution of 600 ps and a secondary value of 200 ps which considered improvements in the detector technology. The image reconstruction code is based on MLEM and probabilities were calculated using ray-tracing based on the Siddon algorithm. We have modified it in order to include time of flight (TOF) information. The simulations of the PET scanner were performed with Gate 6.1. The initial design of the CC is made up of six layers (CC-6) of $LaBr_3$ crystal (dimensions 1x20x20 cm3), separated by 10 cm. An alternative configuration has been considered where the six layers are arranged in two sectors (CC-3+3). The scintillator crystals are read out by Silicon Photomultipliers. The data have been reconstructed using MLEM code adapted for Compton imaging considering two and three interaction events. The simulations for the Compton Camera have been done with Geant4.9.3. The CC is situated perpendicular to the beam axis.

From the images of the individual reconstructed positron distribution and prompt-gamma distribution, we have calculated the range of the distribution defined as 50% of the maximum at the distal edge. The difference between calculated and the reference range (obtained from the original source at 160 MeV) is shown in figure 1. From this plot one can see that TOF has little effect on range calculation. Considering the different configurations, the one with the lowest sensitivity (PR-PET-60) does not reproduce the 3-mm difference between consecutive energies. Related with the CC images, the configuration of the 3+3 is the one that shows better range assessment. In short term, patient studies will be included in the study for a complete evaluation of such imaging systems.

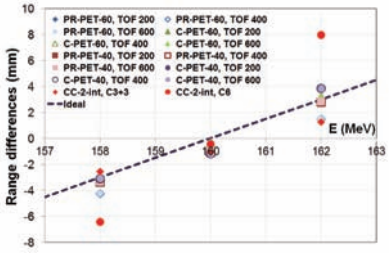

Figure 1. Range differences for reconstructed images generated by proton beams for all the studied imaging systems (PET and CC) and geometries.

References

[1] W. Enghardt et al. Nucl. Instr. Phys. Res. A 525 (2004) 284

[2] CH. Min et al. App. Phys. Lett 89 (2006)

[3] G. Llosá et al. Nucl. Instr. And Meth. A 718 (2013) 130

ENVISION Project

- European NoVel Imaging Systems for ION therapy

on-line dose monitoring by developing novel imaging modalities related to dose deposition that allow to assess the treated volume during hadrontherapy

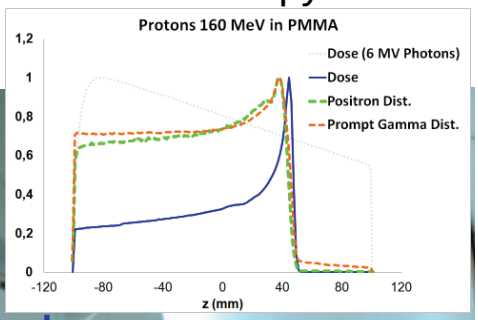

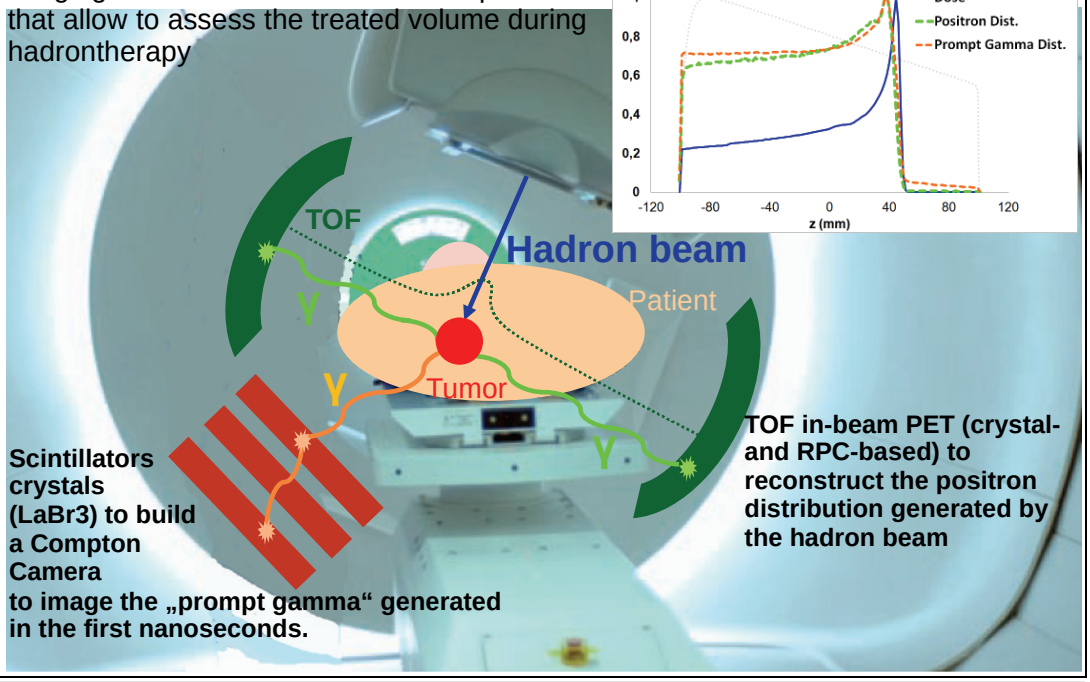

Scintillators crystals (LaBr3) to build a Compton Camera to image the „prompt gamma“ generated in the first nanoseconds.

TOF in-beam PET (crystal- and RPC-based) to reconstruct the positron distribution generated by the hadron beam

PIPA
05.11.13
I. Torres

ToF-PET and Compton Camera

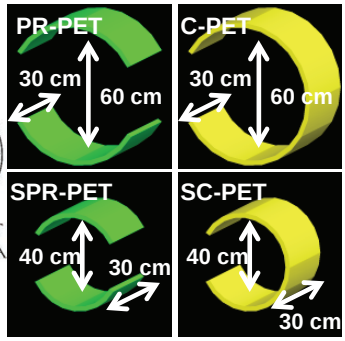

PET: Best images are obtained for the lowest TOF and C-PET with 40 cm diameter**. TOF has little effect on the range calculations**. The configuration with the lowest sensitivity (PR-PET-60) does not reproduce the 3-mm difference between consecutive energies. **Compton Camera:** As expected the 2-interaction images are better (high efficiency). The 3+3 configuration shows improved images and range estimation due to higher sensitivity and better solid angle coverage

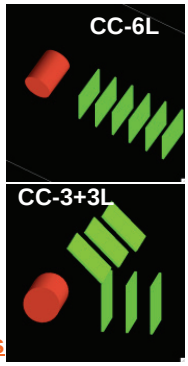

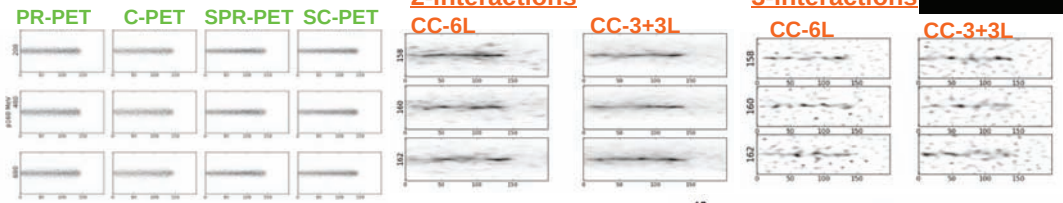

Carbon-ion treatment patient

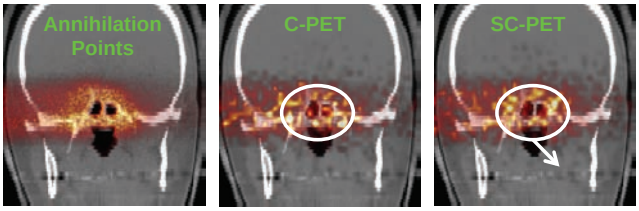

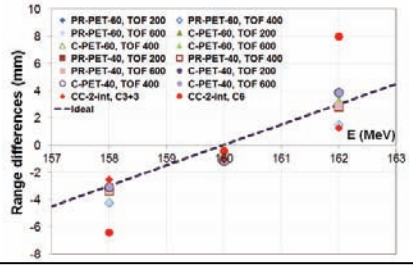

PIPA
05.11.13
I. Torres

Development of a Three Layer Compton Telescope Prototype Based on Continuous $LaBr_3$ Crystals and Silicon Photomultipliers

Marco Trovato[1], J. Barrio[1], P. Botas[1], J. Cabello[1], J. E. Gillam[1], C. Lacasta[1], J. Oliver[1], M. Rafecas[1,2], C. Solaz[1], P. Solevi[1], V. Stankova[1], I. Torres-Espallardo[1] and G. Llosá[1]

[1] Instituto de Fisica Corpuscular, Universitat de Valencia/CSIC, Spain, E-mail: marco.trovato@ific.uv.es

[2] Depto. De Física Atómica, Molecular y Nuclear, Universitat de Valencia, Spain

Introduction

Hadron therapy is a radiotherapy technique which consists in irradiating tumor cells with protons or ions. The interaction of the hadron beam with the tissue produces exited nuclei emitting prompt gamma rays. Compton camera systems can be used to detect those gamma rays and reconstruct the origin of the photons, as required for dose treatment monitoring. A Compton telescope prototype for treatment monitoring in hadron therapy is under development at IFIC - Valencia, in the framework of the European ENVISION project. The prototype will consist of three detector layers and each layer will be made of a continuous $LaBr_3$ crystal coupled to four Silicon Photomultiplier (SiPM) arrays [1], [2].

Experimental Setup and Detector Characterization

A two layer prototype of the telescope has already been built up and tested. Each layer is composed of a 32x36 mm^2 $LaBr_3$ crystal coupled to four SiPM arrays. Each detector is connected to a custom made hybrid board that provides mechanical support, the bias for the MPPC arrays and also hosts a VATA64HDR16 ASIC from Gamma Medicas-Ideas, employed to read-out the 64 detector channels. Each hybrid board is connected to a data acquisition system (DAQ) developed at IFIC and equipped with an FPGA that provides the configuration for the ASIC and the control of the acquisition process [3]. The detectors employed in the prototype have been characterized in terms of energy and spatial resolution. Fig. 1 shows a ^{22}Na energy spectrum obtained with the 32x36x5 mm^3 $LaBr_3$ crystal. A Gaussian fit to the 511 keV photopeak results in an energy resolution measurement of 7.4% FWHM. Position estimation methods have been tested and the spatial resolution achieved is around 1.4 mm FWHM [4].

System Tests

System tests have been carried out placing the two detectors 41 mm apart and a ^{22}Na source 49 mm far from the first detector. Photons emitted by the ^{22}Na source that are Compton scattered in the first detector and interact also in the second, have been collected. The sum of the energy recorded in both detectors when operating in coincidence shows the expected energy spectrum of a ^{22}Na source with the 511 keV and 1275 keV photopeaks (Fig. 2). Images have been reconstructed with an ML-EM algorithm, assessing the correct functioning of the prototype (Fig. 3). In-beam tests have been performed at the CNA (Centro Nacional de Aceleradores) in Seville. A cyclotron providing an 18 MeV proton beam, was used to irradiate quartz and graphite targets. The processing of the in-beam coincidence data is ongoing. A third detector layer of the telescope, made of a 27.2x26x5 mm^3 $LaBr_3$ crystal, coupled to four SiPM arrays is being assembled.

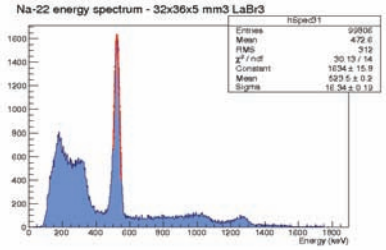

Fig. 1. ^{22}Na energy spectrum obtained with the 32x36x5 mm^3 $LaBr_3$ crystal coupled to four SiPM arrays.

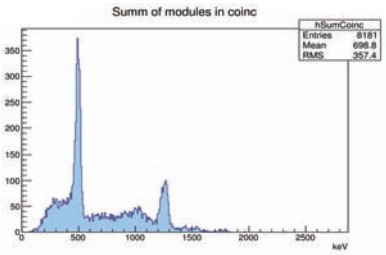

Fig. 2. Sum of the energies deposited in the two detectors operated in coincidence for the ^{22}Na source.

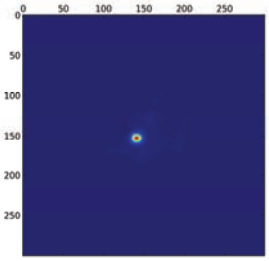

Fig. 3. Image reconstructed of a point-like ^{22}Na source.

References

[1] Roellinghoff et al., Nucl. Inst. And Meth. A 648 (2011) S20-S23.

[2] G. Llosá.et al., Nucl. Inst. And Meth. A 718 (2013) S 130

[3] V. Stankova et al., IEEE NSS-MIC, 2012, pp 1069-1071.

[4] J. Cabello, 2011 IEEE NSS-MIC, pp 3911-3916.

Development of a Three Layer Compton Telescope Prototype Based on Continuous $LaBr_3$ Crystals and Silicon Photomultipliers

M. Trovato, J. Barrio, P. Botas, J. Cabello, J. E. Gillam, C. Lacasta, J. Oliver, M. Rafecas, C. Solaz, P. Solevi, V. Stankova, I. Torres and G. Llosá

IRIS group - Image Reconstruction, Instrumentation and Simulations for medical imaging applications - IFIC/CSIC-UV

✓ The Compton telescope will consist of three detector layers and each layer will be made of a continuous $LaBr_3$ crystal coupled to four silicon photomultiplier (SiPM) arrays

✓ Each detector is connected to a data acquisition (DAQ) board developed at IFIC and used to control the acquisition process

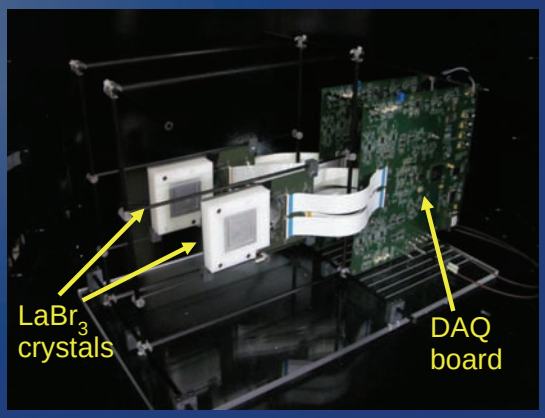

Development of a Three Layer Compton Telescope Prototype Based on Continuous $LaBr_3$ Crystals and Silicon Photomultipliers

✓ A third detector layer of the telescope, made of a 27.2x26.8x5 mm^3 $LaBr_3$ crystal coupled to four SiPM arrays, has been assembled and tested.

✓ Coincidence tests have been carried out with a prototype made of two detector layers, each one composed of a 32x36 mm^2 $LaBr_3$ crystal coupled to four SiPM arrays

✓ Images of a ^{22}Na point-like source have been recontrstructed employing a ML-EM algorithm, determining the correct functioning of the prototype

✓ In-beam tests have been carried out, using a 18 MeV proton beam, irradiating graphite and quartz targets;

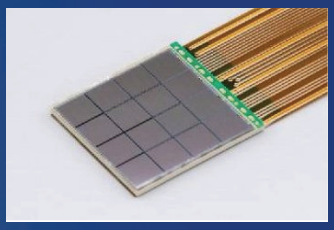

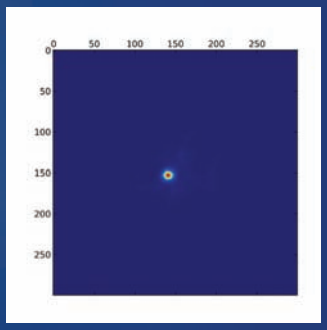

Marco Trovato – IRIS group - IFIC/CSIC-UV

PIPA 2013 - NIRS Workshop on PET Imaging Physics and Applications

Real-time OpenPET imaging system toward PET-guided tumor tracking radiation therapy

Hideaki Tashima[1], Eiji Yoshida[1], Tetsuya Shinaji[2,1], Haruhiko Futada[3], Takeshi Nagata[3], Hideaki Haneishi[2], Taiga Yamaya[1]

[1] National Institute of Radiological Sciences, Japan, tashima@nirs.go.jp,

[2] Chiba University, Japan, [3] Mizuho Information & Research Institute, Japan

We are developing the OpenPET, which can provide an open space observable and accessible to the patient during positron emission tomography (PET) measurement [1], [2]. The OpenPET enables integration of treatment and diagnosis. The most attractive and realistic candidate application is in combination with radiation therapy. OpenPET imaging during particle therapy such as carbon beam treatment has the potential to visualize the irradiation field of a patient. In addition, as a more challenging application, we are focusing on tumor tracking by means of PET, which is conventionally done by marker implantation and X-ray imaging (Fig. 1).

In this study, we proposed a real-time imaging system for the OpenPET as we work toward implementing the PET-guided tumor tracking radiation therapy and we demonstrated its tracking ability using a point source and a small OpenPET prototype [3]. The system employed 3D dynamic row-action maximum likelihood algorithm (DRAMA) and implemented on graphical processing unit (GPU). Figure 2 shows the demonstration setup, captured PC screen during tracking demonstration, and extracted point source positions on the captured screen. The point source was moved according to the sine curve with a cycle of 30 s. The frame rate of the real-time imaging system was 2.0 frames per second. As a result of sine curve fitting, the average delay was 2.1 s.

In addition, we conducted Monte Carlo simulation to assess conditions under which the tumor tracking is feasible using ^{18}F-FDG in a human body scale. Figure 3 shows the simulation result of the tumor tracking with various tumor size and standardized uptake value (SUV). We assumed that the OpenPET measurement was started 100 minutes after the ^{18}F-FDG injection of 370 MBq. The time window was 0.5 s. As a result, we showed that the tumor tracking is feasible if the tumor contains sufficient radioactivity in the case of lung cancer.

Although we have demonstrated real-time tumor tracking using a small OpenPET prototype, further improvement is necessary for applying to the human-sized OpenPET. Therefore, we are developing faster image reconstruction system using a multi-GPU platform and region-of-interest reconstruction technique to minimize image matrix size keeping spatial resolution. In addition, we are developing a time delay correction method using the signal from an additional external device.

References

[1] T. Yamaya, et al., PMB, vol. 53, pp. 757-73, 2008.

[2] T. Yamaya, et al., PMB, vol. 56, pp. 1123-37, 2011.

[3] H. Tashima, et al., IEEE TNS, vol. 59, pp. 40-6, 2012.

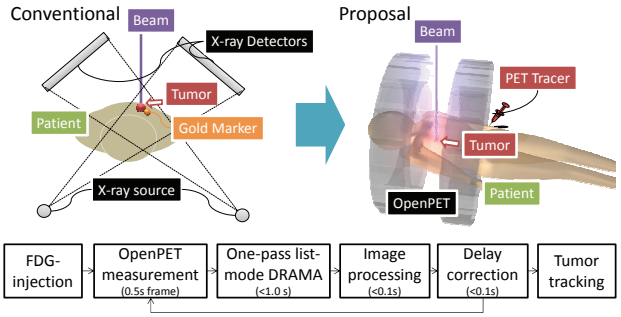

Figure 1. Conceptual illustration of PET-guided tumor tracking radiation therapy and flow chart of the tumor tracking by the OpenPET.

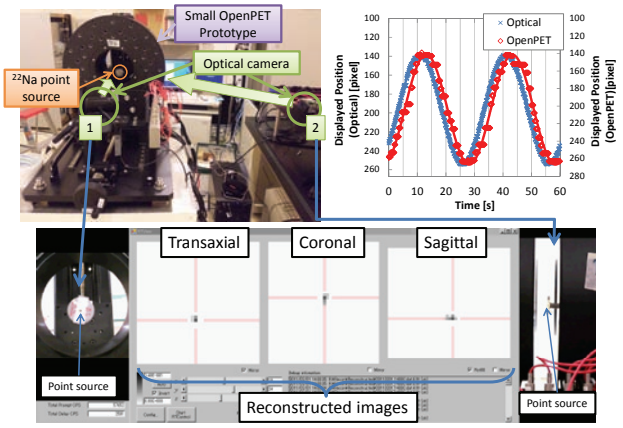

Figure 2. Point source tracking demonstration by the real-time OpenPET imaging system implemented on the small OpenPET prototype.

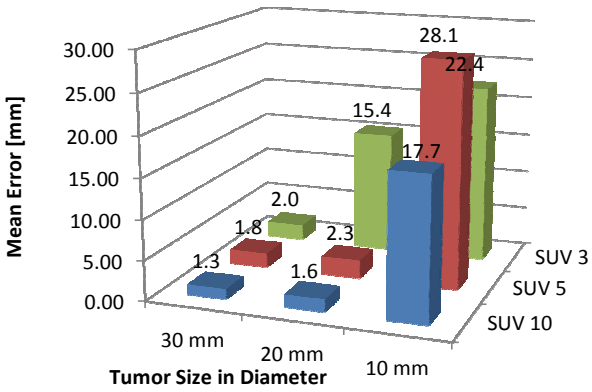

Figure 3. Simulation result of lung tumor tracking by the human-sized OpenPET using Gate simulation toolkit and XCAT whole body human phantom

Real-time OpenPET imaging system toward PET-guided tumor tracking radiation therapy
Tashima et al.

Real-time Imaging System for the OpenPET

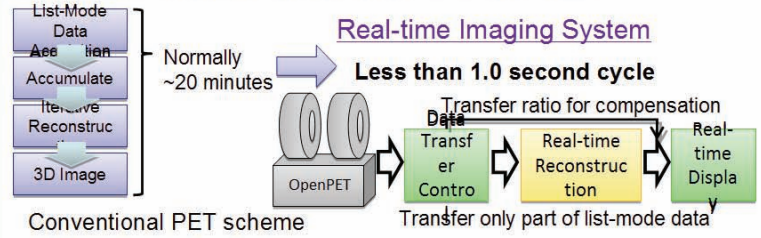

Demonstration of the point source tracking by the small OpenPET prototype

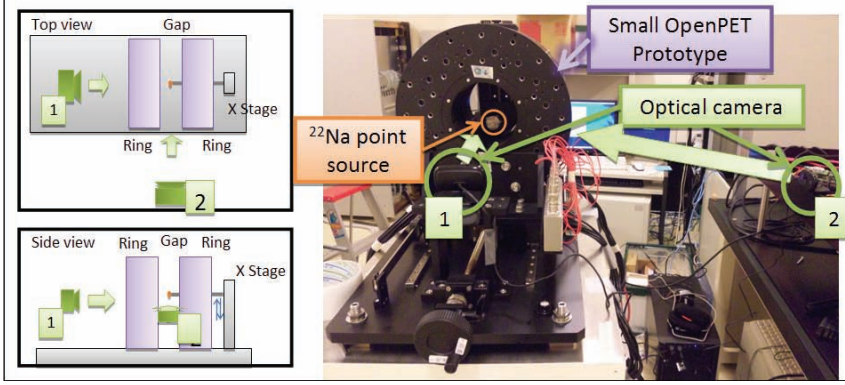

Captured screenshot during tracking demonstration

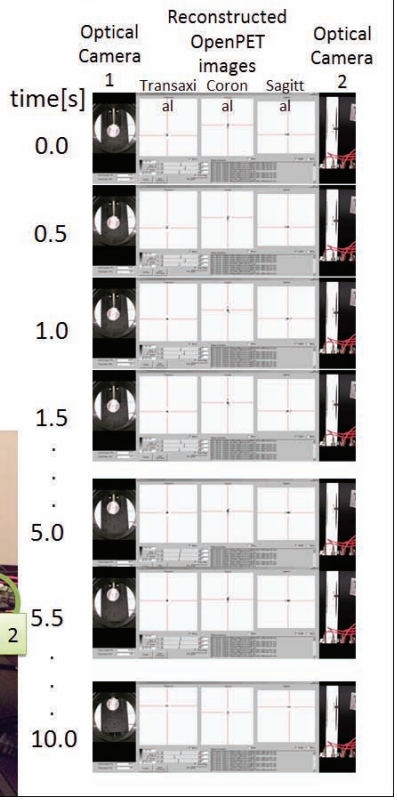

Feasibility study of the tumor tracking in the human with ^{18}F-FDG

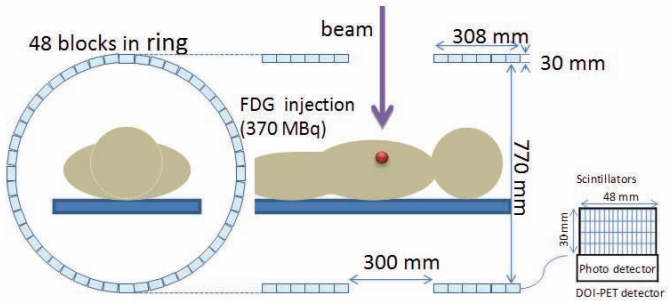

Simulation geometry

Average tracking error

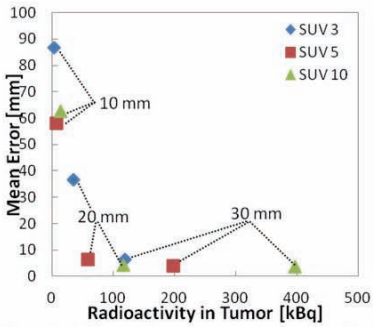

Radioactivity in tumor was calculated from tumor size and SUV

Final Tumor Tracking System Workflow

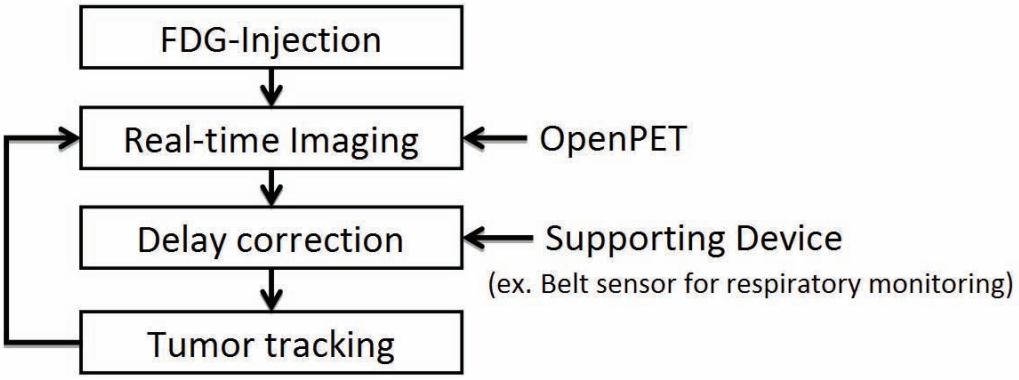

Performance improvement of GPU image reconstruction for OpenPET

Haruhiko Futada[1], Takeshi Nagata[1], Hideki Tashima[2], Eiji Yoshida[2], Taiga Yamaya[2]

[1] Mizuho Information & Research Institute, Japan, haruhiko.futada@mizuho-ir.co.jp,

[2] National Institute of Radiological Sciences, Japan

1. Introduction

The OpenPET, which we have been developing in NIRS, has the potential to enable new PET applications such as image-guided radiation therapy. To achieve this, real-time imaging system was proposed [1]. The system uses a graphics processing unit (GPU) for the image reconstruction and has capability to reconstruct images at 2 frames per second. However, further speed improvement is necessary. In this research, we try to improve reconstruction speed by implementing the GPU-suitable method.

2. Method

Image Reconstruction Method

We use the list-mode DRAMA for image reconstruction. The formula is given by

$$x_j^{(k,l+1)} = x_j^{(k,l)} + \lambda^{(k,l)} \frac{x_j^{(k,l)}}{G_{lj}} \sum_{t \in S_l} a_{i(t)j} \left(\frac{1}{\sum_{j'=1}^{J} a_{i(t)j'} x_{j'}^{(k,l)}} - p_{lj} \right),$$

$$p_{lj} = \sum_{i=1} a_{ij} \Big/ \left(\sum_{l=1}^{L} \sum_{t \in S_l} a_{i(t)j} \right),$$

$$G_{lj} = \max_{l} \sum_{t \in S_l} a_{i(t)j} p_{lj},$$

where l is subset index ($l = 1,\ldots,L$), k is the iteration index ($k = 1,\ldots,K$), i (t) is the LOR index at which the t-th event is detected, S_l is the set of event index t in the l-th subset, x_j is the value of the j-th voxel, a_{ij} is the system matrix element, λ is the relaxation parameter, G_{lj} is the normalization matrix element, and p_{lj} is the blocking factor.

GPU Implementation

We use the ray-driven method for both forward projection and back projection to match the system matrix. CUDA is used to implement the code.

In this research, we combine the two following GPU parallelization.

1) Line partitioning by orientation [2]: In order to reduce thread divergence, the LORs are grouped into two classes according to their predominant direction, and the different CUDA kernels are used for the two classes.
2) LOR parallelization [1]: In the common method for parallel implementations, each LOR is assigned to separate thread. Furthermore, a LOR is divided by image slices, and is processed in parallel (LOR parallelization).

In general, fine level tuning is necessary for GPU programming. In this research, we use shared memory tuning (using shared memory as reconstruction image cache) and fastmath.

Table 1. Processing time comparison

Number of LORs	Method	Processing time [sec.]
1,000,000	Method in the current system (LOR parallelization is used. Line partitioning by orientation is NOT used.)	23.69
	Proposed method (LOR parallelization is used. Line partitioning by orientation is used)	1.58

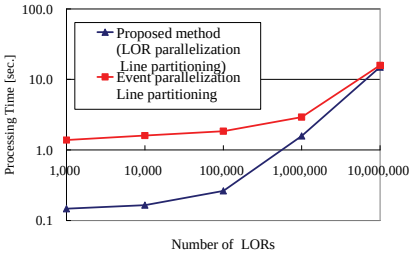

Figure 1. Processing time for different number of LORs

3. Experiment and Result

GPU Hardware and Parameters

We used GeForceGTX 580 GPU, which had 512 processor cores. CUDA Toolkit v5.0 was used.

The number of voxels of the reconstructed images was 76x76x84. The number of subsets L was 50. The number of iterations K was 1. We used Gaussian function with the kernel size of 13x13 pixels for modeling the detector response function.

Processing Time

Table 1 shows the processing time comparison of the method in the current system and the proposed method. The processing time for different number of LORs is shown in Figure 1. We have also experimented a method that excluding LOR parallelization from the proposed method here. The result shows that LOR parallelization keeps lower overhead for small number of LORs.

4. Conclusion

GPU-suitable reconstruction method was proposed and examined. Future work is to embed the proposed method to the actual real-time imaging system.

References

[1] Tashima, Hideaki, et al. "Real-time imaging system for the OpenPET." *IEEE Transactions on Nuclear Science* 59.1 (2012): 40-46.

[2] Cui, Jing-yu, et al. "Fully 3D list-mode time-of-flight PET image reconstruction on GPUs using CUDA." *Medical physics* 38.12 (2011): 6775-6786.

- **Background**
  - We are developing OpenPET at NIRS.
  - Real-time imaging system for OpenPET was proposed.
    - For image reconstruction, Graphics processing unit (GPU) is used
      - Feature of GPU:
        - » Many-core processor.
        - » High theoretical performance.
        - » GPU program performance heavily depends on the implementation.

GPU

    - Frame rate of current system is 2 fps.
      - Performance improvement is necessary.

- **Purpose**
  - Improving reconstruction speed by implementing the GPU-suitable method.

- **Method**
  - Parallelizing list-mode DRAMA in a suitable form for GPU.

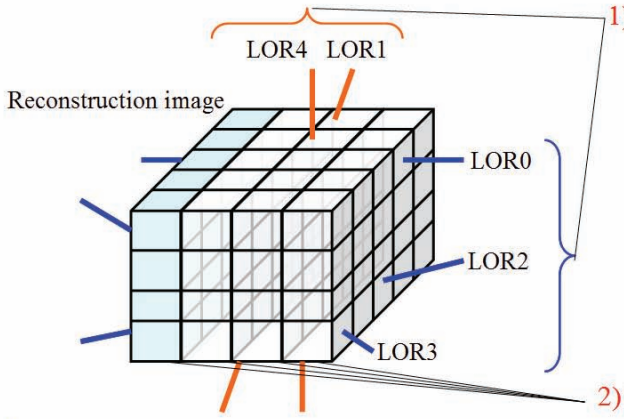

1) Line partitioning by orientation
- LORs are grouped according to their direction
- Grouped LORs are processed separately to use fast memory efficiently

2) LOR parallelization
- LOR is divided by image slices and processed in parallel

- **Result**
  - 14 times faster than method in the current system (comparison of purely reconstruction time).
  - keeps lower overhead for small number of LORs.

Time-based pulse signal processing and multiplexing method for frontend electronics

Hiroyuki Takahashi[1], Kenji Shimazoe[2], Tadashi Orita[2], Jianyong JIANG[2]

[1] Faculty of Engineering, The University of Tokyo, Japan, leo@n.t.u-tokyo.ac.jp, [2] Faculty of Engineering, JAPAN

PET requires a multichannel spectroscopy system. Conventional PET systems rely on analogue position coding method such as a charge division method although an individual readout method can manage a very high counting rate without distortion of image. Because it is not very easy to integrate huge number of channels, a digital frontend system is not effectively used so far. Our first motivation was to realize an intelligent waveform signal processing system, which can deal with a waveform multiplexing principle [1]. Figure 1 shows a principle of waveform multiplexing scheme. We on purpose alter the decay time of the pulse belonging to each readout channel. This approach could share many detectors in each fast ADC channel.

Recently theTime-over-Threshold method is studied where the use of time width is a new approach to very compact and power-efficient system. Thus, it could be used for multi-channel energy resolving systems. One further approach to more compact front-end electronics is shown in Figure 2. The ToT pulse is followed by two subsequent pulses whose pulse widths show an address of the multiplexed channel. We call this method a pulse train method. The ToT method can open a door to very compact front-end electronics system, however, it suffers from nonlinearity of pulse width vs. deposited energy. Our dynamic time-over-threshold method improves the linearity between the pulse width and the pulse height well below 1 %, which is sufficient for most cases. Direct digitization of signal at the front-end makes a complicated multichannel imaging system feasible. We further explore digital division method within a pixel framework. A new approach is to use a silicon photomultiplier and combine sub-pixel readout channels. A pulse width encoding system well suits to such a high-spacial-resolution system.

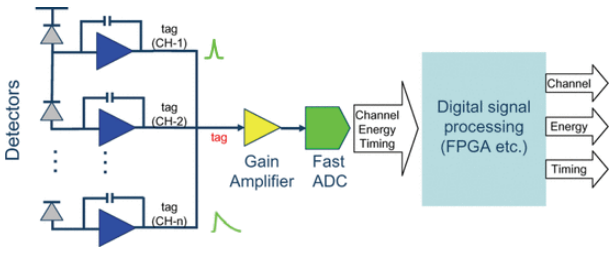

Figure 1. Waveform multiplexing principle.

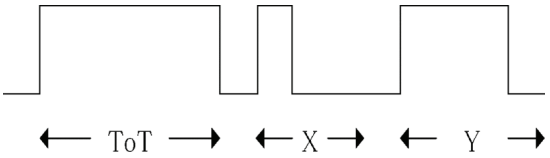

Figure 2. Pulse train including energy, X-address, and Y-address.

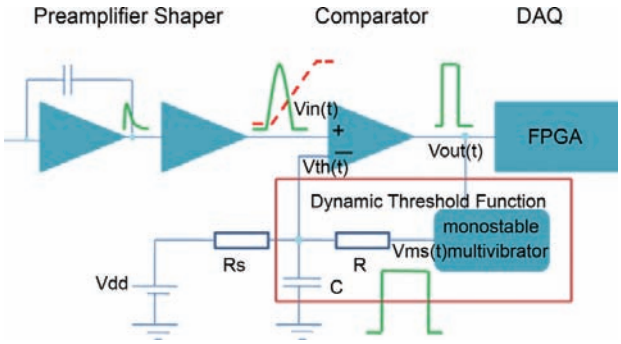

Figure 3. Schematic diagram of the dynamic Time-over-Threshold method.

References

[1] "Development of Waveform Multiplexing Method With Decay Time Modulation for Front-End ASIC of Pixelated Detectors", B. Shi, K. Shimazoe, Y. Wang, T. Fujiwara, H. Takahashi, and N. Iyomoto, IEEE Trans. on Nuclear Science, NS-58, No.4, 2019-2023 (2011).

[2] "Novel Front-End Pulse Processing Scheme for PET System Based on Pulse Width Modulation and Pulse Train Method", Kenji Shimazoe, Hiroyuki Takahashi, Boxuan Shi, Tetsuo Furumiya, Junichi Ooi, Yoshihiko Kumazawa, and Hideo Murayama, IEEE Trans. on Nuclear Science, NS-57, No.2, 782-786 (2010).

[3] "Dynamic Time Over Threshold Method", Kenji Shimazoe, Hiroyuki Takahashi, Boxuan Shi, T. Orita, Tetsuo Furumiya, Junichi Ooi, and Yoshihiko Kumazawa, IEEE Trans. on Nuclear Science, NS-59, No.6, 3213-3217 (2012)

10 ch Waveform Sampling ASIC
& Waveform Multiplexing

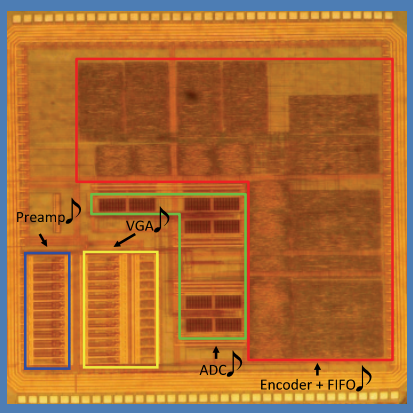

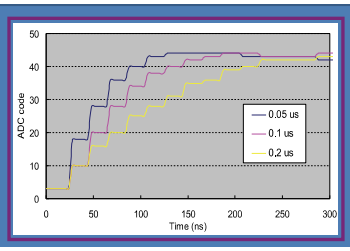

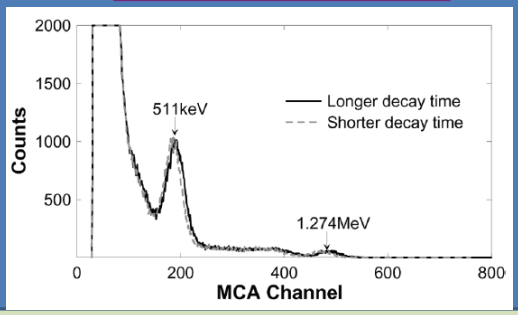

12 Ch Pulse Train ASIC

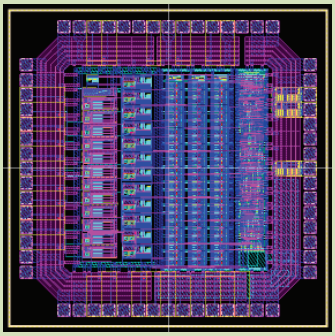

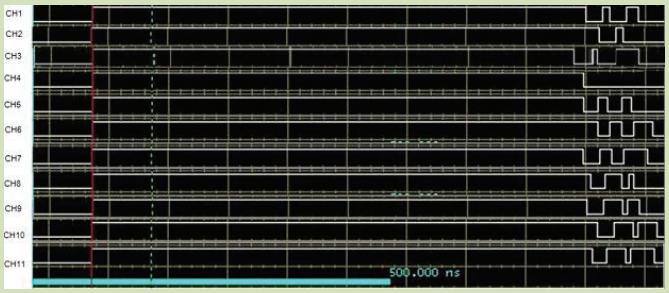

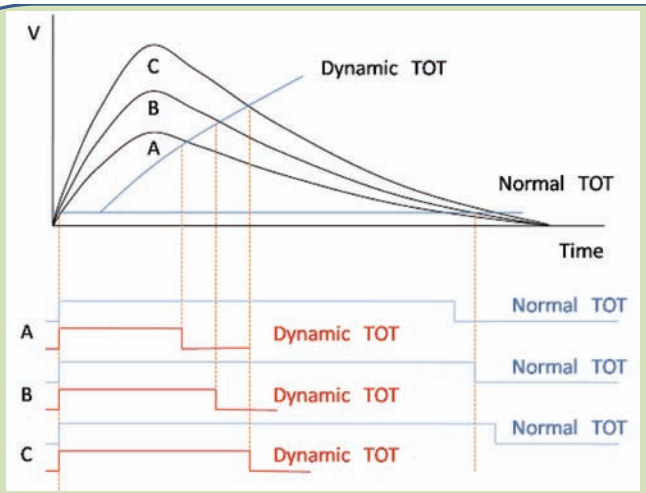

Principle of Dynamic Time-over-Threshold Method

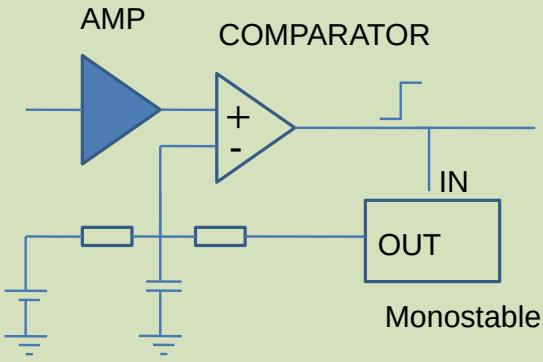

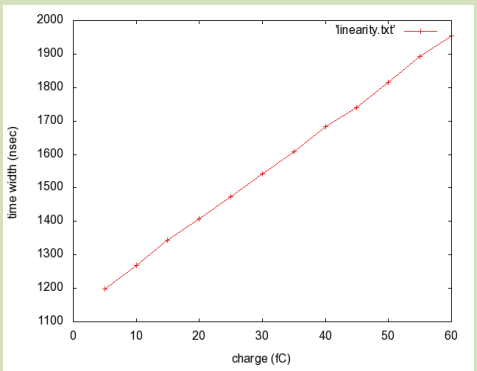

Linearity

Recent Results in SiPM-Based Detectors for Time-of-Flight PET and Their Promise for In-Beam PET and Prompt Gamma Ray Imaging

Dennis R. Schaart

[1] Delft University of Technology, The Netherlands, d.r.schaart@tudelft.nl

The use of time-of-flight (TOF) information in positron emission tomography (PET) has been shown to enable significant improvement in image noise properties, especially in larger patients. Silicon photomultipliers (SiPMs) are solid-state photosensors offering high internal gain while being compact, essentially transparent to gamma rays, and insensitive to magnetic fields. Since several years a number of manufacturers are offering reliable and practical devices. This has spurred many research groups to explore their potential use in scintillation detectors for PET, aiming at e.g. compactness, high spatial resolution, depth-of-interaction (DOI) correction, MRI-compatibility, and improved TOF performance. At the same time, SiPM technology itself is undergoing rapid development. For example, a fully digital implementation of the SiPM, the so-called digital photon counter or dSiPM, has been introduced recently. SiPMs and dSiPMs enable excellent timing resolution, with coincidence resolving times (CRTs) well below 200 ps FWHM having been demonstrated by several groups already. This paper presents an overview of recent developments in dSiPM-based PET detectors as well as an outlook on the potential impact of these results on in-situ PET and prompt gamma imaging for particle therapy treatment monitoring. It is discussed how the favorable properties of SiPMs and dSiPMs can be exploited to provide realistic solutions for in-vivo particle therapy monitoring concepts proposed by various groups in recent years. In particular, it is shown how the excellent timing performance of dSiPM based scintillation detectors can be used to improve sensitivity and to reduce artifacts of in-situ PET devices, as well as to reduce background noise in prompt gamma imaging.

Monolithic scintillator performance summary

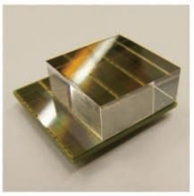
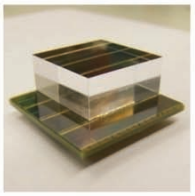

Current results with LSO monolithic scintillators on dSiPM arrays:

Performance parameter		Monolithic	State of the art
Energy resolution	(% FWHM)	**11 - 12**	~12
Spatial resolution	(mm FWHM)	**1.0 - 1.6**	4 - 6
DOI resolution	(mm FWHM)	**3 - 5 mm**	None
CRT	(ps FWHM)	**160 - 185**	500 - 650

⇒ A highly promising detector for future clinical PET/CT and PET/MRI systems

TU Delft Dennis R. Schaart
Delft University of Technology

- H.T. van Dam et al, Phys Med Biol 58, 3243-3257, 2013
- S. Seifert et al, Phys Med Biol 58, 3061-3074, 2013

SUBLIMA

In-situ dose imaging

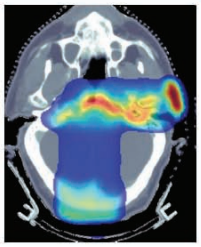

In-situ dose delivery monitoring

Incentive

Use novel detector technology under development for PET/MRI at TU Delft, to realize a clinically useful in-situ device for dose delivery monitoring

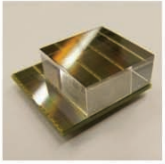
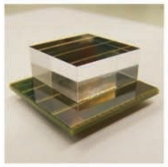

www.sublima-pet-mr.eu

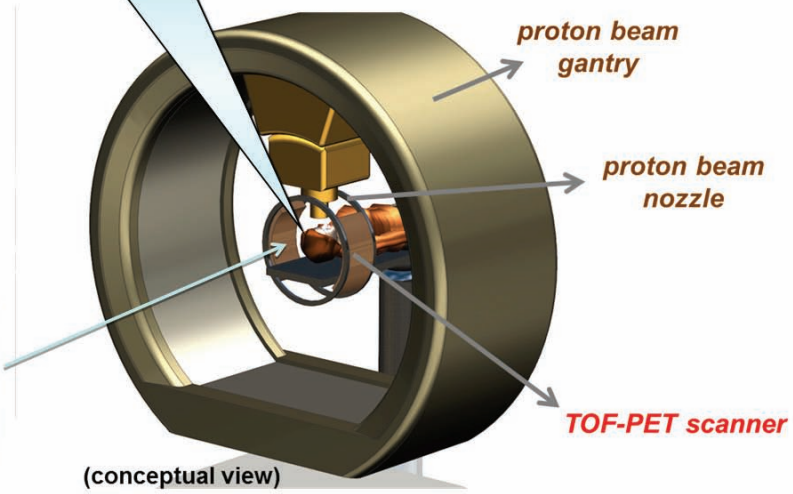

(conceptual view)

HollandPTC

Images: SUBLIMA project (Philips-Delft) & ISoToPE project (Delft-Groningen)

medical delta · Erasmus MC Universitair Medisch Centrum Rotterdam · LUMC Leids Universitair Medisch Centrum · TU Delft

X'tal cube: 3-dimensional position sensitive PET detector

Naoko Inadama[1], Yoshiyuki Hirano[2], Fumihiko Nishikido[2], Munetaka Nitta[3], Taiga Yamaya[2]

[1] NIRS, Japan, inadama@nirs.go.jp, [2] NIRS, Japan, [3] Chiba University, Japan

To achieve high spatial resolution in all 3 dimensions on a PET detector, we have developed the DOI detector named X'tal cube. Structure of the X'tal cube is shown in Figure 1a). Since a multi-pixel photon counters (MPPC) is small enough not to interfere with radiations, the X'tal cube has MPPCs on all six sides of a scintillation crystal block. The crystal block are then segmented into cubes by only optical discontinuity so that scintillation light originating in a segment spreads to all 3 dimensions and is detected by the MPPCs at all six surfaces of the crystal block. Figure 1b) is the 3 dimensional (3D) position histogram obtained by the irradiation of 511 keV gamma-rays from ^{22}Na sources to an X'tal cube [1]. The X'tal cube was consisted of a LYSO crystal block segmented 3-dimensionally into an 18 × 18 × 18 array of 1 mm × 1 mm × 1 mm cubes by laser processing [2]. The histogram represents the results of an Anger-type calculation using all MPPC signals for all events and crystal segment responses are formed by the results in it. Figure 1c) shows a 2D position histogram for a central segment layer extracted from the histogram in Figure 1b). It shows clear discrimination of most 18 × 18 responses but some corner responses and that indicates capability of the X'tal cube for 1 mm spatial resolution in all 3 dimensions. We found in further study that optimization in the Anger-type calculation improves the segment identification performance as shown in Figure 1d) which represents the same responses as Figure 1c).

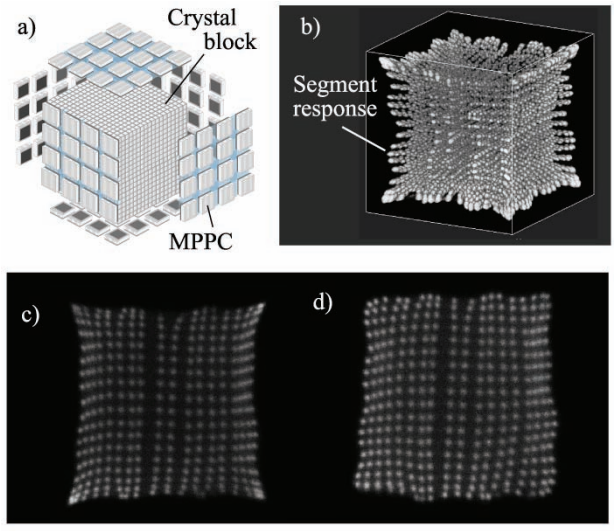

Figure 1. a) Structure of the X'tal cube. b) 3D position histogram obtained by the X'tal cube including a crystal block segmented into cubes 1 mm on each side. c) 2D position histogram corresponding to the 5th-layer of the X'tal cube. d) The same 2D position histogram as c) but with optimized Anger-type calculation.

As the next step, we tried 2-sides readout on the X'tal cube for a compact shape to gain packing fraction of a PET system [3]. We confirmed so far that segment identification was possible by only 2-sides readout, the top and bottom surfaces of the crystal block, for the LYSO crystal block segmented into a 6 × 6 × 6 array of 3 mm × 3 mm × 3 mm cubes by laser processing. Figure 2a) is the 3D position histogram obtained by the irradiation of 511 keV gamma-rays to the X'tal cube. Figure 2b) is a 2D position histogram extracted from Figure 2a) and responses in it are corresponding to 6 × 6 segments in a central layer of the crystal block. These figures prove enough segment identification performance.

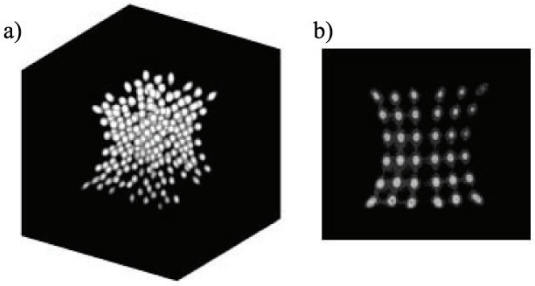

Figure 2. a) 3D position histogram obtained by the X'tal cube including a crystal block segmented into cubes 3 mm on each side. b) 2D position histogram corresponding to the 3rd-layer of the X'tal cube.

For energy performance, we obtained comparable energy resolution between a central segment and an outer segment for both the X'tal cubes mentioned above. The next study will be the measurement of time resolution, which much depends on the data acquisition system.

References

[1] E. Yoshida, Y. Hirano, H. Tashima, N. Inadama, F. Nishikido, T. Moriya, T. Omura, M. Watanabe, H. Murayama, H. Ito, and T. Yamaya, "A Impact of the laser-processed X'tal cube detector with 1 mm isotropic resolution in PET imaging," *IEEE NSS MIC CR.*, M16-15, Anaheim, California, 2012.

[2] T. Moriya, K. Fukumitsu, T. Sakai, S. Ohsuka, T. Okamoto, H. Takahashi, M. Watanabe, and T. Yamashita, "Development of PET detectors using monolithic scintillation crystals processed with sub-surface laser engraving technique," *IEEE Trans. Nucl. Sci.*, Vol. 57, No. 5, pp. 2455-2459, Oct. 2010.

[3] Y. Hirano, N. Inadama, E. Yoshida, F. Nishikido, H. Murayama, M. Watanabe, and T. Yamaya, "Potential for reducing the numbers of SiPM readout surfaces of laser-processed X'tal cube PET detectors," *Phys. Med. Biol.* 58, pp. 1361–1374, 2013.

Structure of X'tal cube

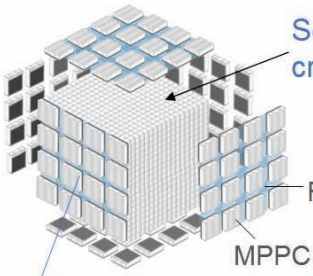

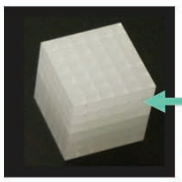

Segmented 3-dimensionally

No reflector inside

Only optical discontinuity

radiation

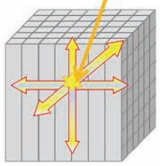

Scintillation light is spread in 3 dimensions and detected from all surfaces

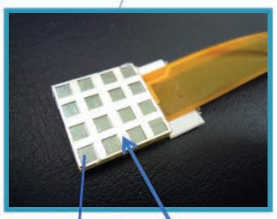

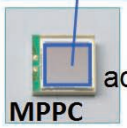

Reflector

active area

We prepared two X'tal cubes for performance evaluation

	XC-1	XC-2
Scintillator	LYSO ($18 \times 18 \times 18$ mm^3)	
Segment size	$1 \times 1 \times 1$ mm^3	$3 \times 3 \times 3$ mm^3
Segment number	$18 \times 18 \times 18$	$6 \times 6 \times 6$
MPPC	S10931-050P, 3×3 mm^2 active area, 4×4 MPPCs /side	
	6-side readout (96 MPPCs)	2-side readout (32 MPPCs)

Crystal block

Laser

Segmented by 3D laser processing

Light guides were NOT used.

By Hamamatsu Photonics K.K., Japan

XC-1 (6-side readout)

We confirmed the ability of the X'tal cube for 1 mm spatial resolution in all 3 dimensions.

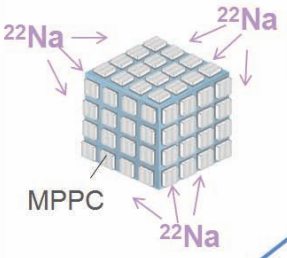

5832 segments

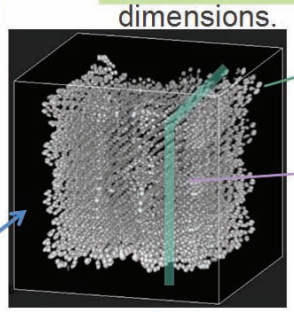

3D position histogram

Segment response

Extracted

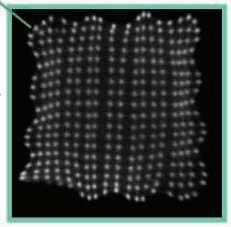

2D position histogram

Sufficient identification of 1 mm x 1 mm x 1 mm segments

XC-2 (2-side readout)

We confirmed the ability of the X'tal cube for 3 mm spatial resolution in all 3 dimensions so far.

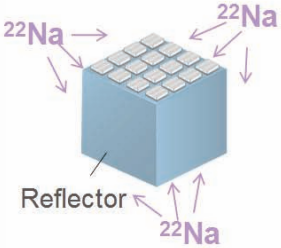

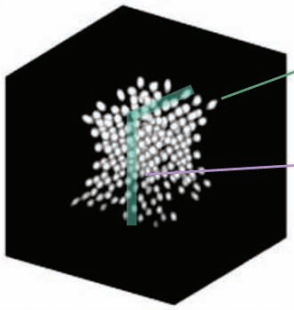

3D position histogram

Segment response

Extracted

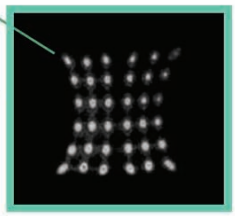

2D position histogram

Sufficient identification of 3 mm x 3 mm x 3 mm segments

An asymmetric PQS detector-block design for a gapless PET detector ring

Hongdi Li, Rocio Ramirez, Yuxuan Zhang, Hossain Baghaei, Wai-Hoi Wong

Department of Cancer Systems Imaging, the University of Texas, M. D. Anderson Cancer Center, Houston, Texas, USA,

gwong@mdanderson.org

We have proposed a gapless PET detector ring concept base on the PMT-quadrant-sharing (PQS) detector block [1], as shown in Figure 1. The cubic block is ground on three surfaces to form a symmetric shape with a pentagon cross-section. With this type of blocks, a continuous gapless detector ring can be built, which has been adapted in two preclinical PET systems, RRPET [2] and MuPET [3].

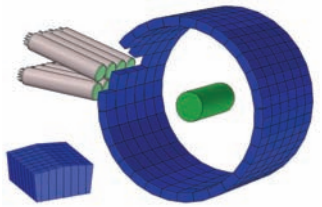

Figure 1. Gapless detector ring using pentagon shape detectors.

A human wholebody PET system has much more blocks than preclinical PET. Thus we developed a new version of the PQS gapless detector ring geometry [4] shown in Figure 2. In this design, the ring consists of certain number of detector banks. Each bank is built with symmetric cubic blocks in the middle and two half-ground asymmetric blocks on each side. With this design, the number of surface need to be ground is significantly reduced. For a bank consists of N blocks, the grinding work is reduced to 1/N compared to the original design.

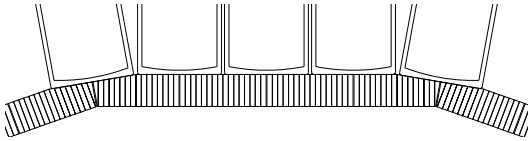

Figure 2. New gapless detector ring geometry with multiple blocks in each bank.

Moreover, the asymmetric block can be further improved shown in Figure 3. For the half-ground block in the PQS-block concept, the top surface is ground to the middle of the block (8 crystal rows be ground for a 16x16 block). When 38-mm round PMTs are used, the wall thickness for the glass tube is about 2 mm and the photo cathode area is smaller than the PMT window, so we can reduce the ground surface without sacrificing the photon collection when PMTs coupled to the ground surfaces. In the less-than-half-ground block, the top surface will be ground for only 6 crystal rows instead of 8. The advantages of the less-than-half-ground block are:

1. Saving on the processing time: The amount of material to be ground away is reduced to 56%.
2. Saving on material: The expensive LSO/LYSO crystal is the major cost of PET. The crystal ground away will be lost. For the less-ground block, material is saved, thereby increasing the sensitivity of the PET system.
3. Simplify the detector decoding mask design. In order to achieve an idea decoding, an asymmetric mask should be used. However, asymmetric mask will increase the manufacture cost of the detector, and may increase the rate of the mistakes during the grinding (ground on the wrong side due to asymmetry). If the asymmetric block can be decoded using the symmetric mask of the symmetric block, the development and production cost can be reduced. With the less-ground block, the asymmetric effect will be less significant and more likely to be able to use the same symmetric mask of the symmetric blocks in the rest of the detector ring.

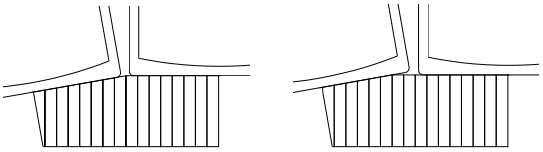

Figure 3. Geometry of two types of asymmetric blocks.

In this study we developed a less-ground asymmetric block based on the symmetric 39-mm 16x16 cubic block developed for a whole-body PET [5]. The decoding map, profiles, energy resolution and peak-to-valley ratio are shown in Figure 4 and Table 1. The results show that the only difference in the asymmetric block is that the decoding map shifts to the un-ground side. However, all crystals are still well separated and will not affect its application.

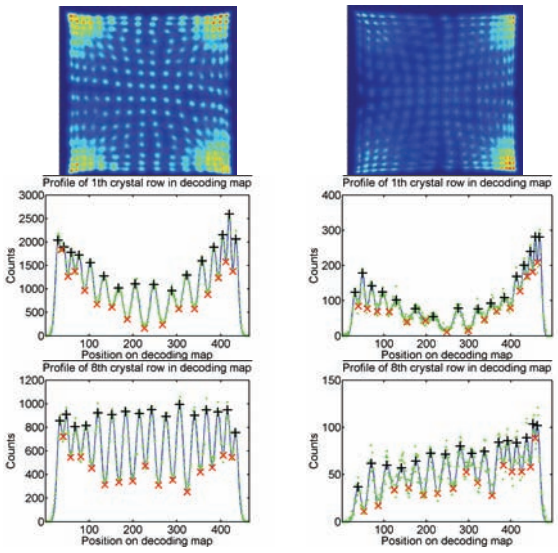

Figure 4. Comparisons of the decoding maps, profiles from the cubic symmetric block (left) and the asymmetric block (right).

Table 1. Detector performance comparison

	Symmetric	*Asymmetric*
Energy resolution range	12.1%~22.6%	12.8%~23.1%
Energy resolution average	14.27%	14.37%
Peak-to-valley ratio	2.10	2.10

References

[1] W-H Wong et al, IEEE TNS, 40, 962-996, 1993.
[2] S. Xie et al, IEEE TNS, 52, 210-216, 2005.
[3] W-H Wong et al, JNM, 53, 1786-1793, 2012.
[4] H. Li et al, IEEE NSS-MIC Conference, 2013, Seoul.
[5] R. Ramirez et al, IEEE NSS-MIC Conference Record, 3794-9796, 2012.

An asymmetric PQS detector-block design for a gapless PET detector ring

Hongdi Li, Rocio Ramirez, Yuxuan Zhang, Hossain Baghaei, Wai-Hoi Wong

The University of Texas, M. D. Anderson Cancer Center, Houston, Texas, USA, gwong@mdanderson.org

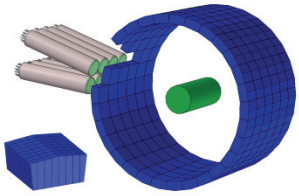

A gapless PET detector ring for small animal PET system (used by our RRPET and MuPET animal PET-CT)

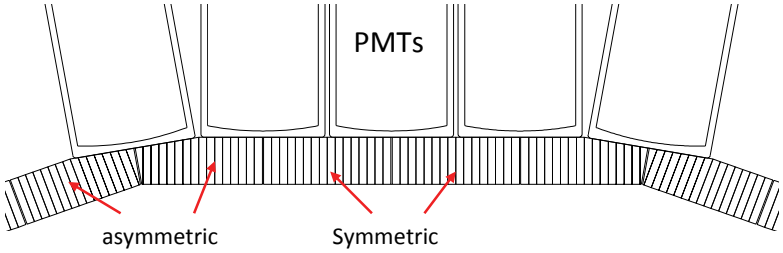

A new gapless detector module concept for big size human systems

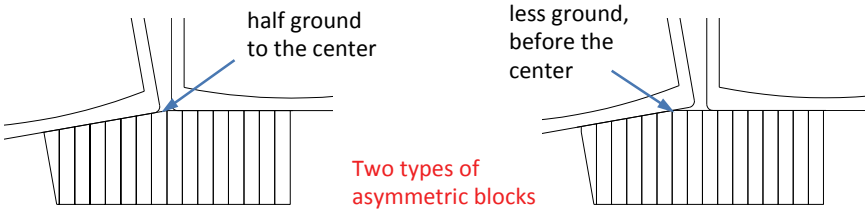

Advantages of the less-ground block:

- saving on the processing time;
- saving on the material;
- increasing on the sensitivity;
- simplifying on the decoding mask design;

Reduce the COST of the development and production.

Comparisons between the symmetric and less-ground asymmetric block:

	Symmetric	*Asymmetric*
Energy resolution range (%)	12.1 ~ 22.6	12.8 ~ 23.1
Energy resolution average (%)	14.27	14.37
Peak-to-valley ratio	2.10	2.10

Decoding maps, profiles of the symmetric block (left) and the asymmetric block (right)

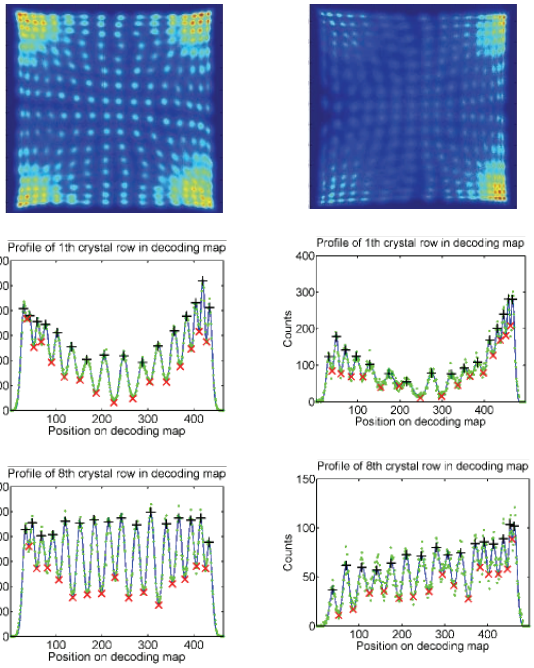

Conclusion: the performance of the less-ground asymmetric detector block is as good the symmetric detector block while improving production cost and sensitivity

MuPET Images of Anesthetized Healthy Mice under Different Conditions

Hossain Baghaei[1], Hongdi Li[1], Yuxuan Zhang[1], Rocio Ramirez[1], and Wai-Hoi Wong[1]

[1]Department of Cancer Systems Imaging, The University of Texas M. D. Anderson Cancer Center, Houston, TX, USA, hbaghaei@mdanderson.org

A preclinical dedicated murine PET camera (MuPET) has been designed and constructed at The University of Texas MD Anderson Cancer Center [1]. The MuPET system is a solid no-gap detector (figure 1) in which photomultiplier tubes are directly coupled to blocks. It has been integrated with a CT camera into a compact gantry (figure 2). The MuPET camera combines the advantages of lower production cost with high-resolution and high-sensitivity. The characteristics of this PET camera have been reported previously [1]. The camera design is based on the PMT-quadrant-sharing technique (210 low-cost 19-mm PMTs were used). The camera has a ring diameter of 16.6 cm and axial field of view of 11.5-cm. The intrinsic spatial resolution of the camera is about 1 mm.

The MuPET camera has been used to study the change in ^{18}F-FDG biodistribution in healthy mice for 2 different anesthesia and fasting conditions. Because of the mice higher basal metabolic rates per body weight than humans, the effect of anesthesia, dietary state and ambient temperature on ^{18}F-FDG biodistribution is expected to be more pronounced than in humans [2]. Previous studies have suggested that isoflurane anesthesia and fasting may improve biodistribution of ^{18}F-FDG for tumor imaging.

Two healthy mice were scanned. The first one was a 25-g female mouse injected with 29 MBq of FDG and 2 hours later was scanned for 20 min. The mouse was anesthetized using intraperitoneal of a ketamine-xylazine-atropine solution. Mouse was kept fasting after FDG injection and was kept warm during the scan. The second mouse, female and weight 28 g, was injected with 17.4 MBq of FDG and scanned 1 hour later for 20 min. The second mouse was anesthetized by isoflurane inhalation anesthesia. The second mouse was also kept warm during the scan but was not fasting. For each study, the mouse was first scanned with PET camera and then with the CT scanner. The PET data were reconstructed using the 3D-OSEM algorithm without scatter or attenuation correction.

Some reconstructed images are shown in figures 3 and 4. Figure 3. shows a sagittal image of the first healthy mouse (anesthetized with ketamine-xylazine-atropine) fused with CT images. Figure 4, shows the transverse and coronal images of the second mouse anesthetized with isoflurane.

A comparison of images of the 2 mice clearly shows the different effects of anesthesia on distribution of FDG tracer in different tissues. Isoflurane anesthesia in nonfasted mouse caused increase of myocardial FDG uptake while the Ketamine anesthesia had the opposite effect on myocardial FDG uptake. We also found that the Harderian glands are also more clearly observable in images of mice anesthetized by isoflurane inhalation anesthesia while kidney and liver were visually better observable for the mouse anesthetized with ketamine-xylazine-atropine solution.

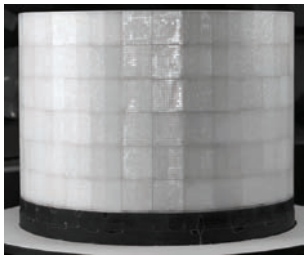

Figure 1. A picture of the solid MuPET detector ring with 30,420 small LYSO crystals (1.24 x 1.4 x 9.5 mm^3) and 78 rings.

Figure 2. A picture of the MuPET gantry.

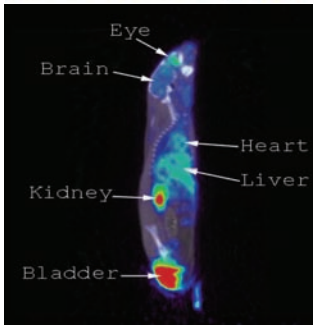

Figure 3. A sagittal image of the first mouse, anesthetized with ketamine, fused with CT images.

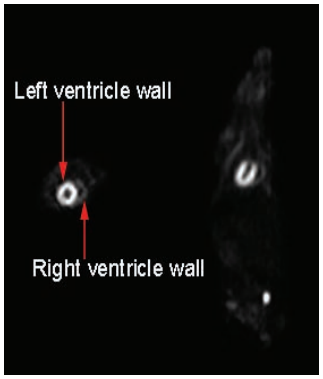

Figure 4. Transverse and coronal images of the second mouse anesthetized with isoflurane.

References

[1] Wong W-H, Li H, Baghaei H, et al. Engineering and Performance (NEMA and Animal) of a Lower-Cost Higher-Resolution Animal PET/CT Scanner Using Photomultiplier (PMT)-Quadrant -Sharing Detectors. *J Nucl Med.* 2012:1786-1793.

[2] Fueger BJ, Czernin J, Hilderbrandt I, et al. Impact of Animal Handling on the results of ^{18}F-FDG PET Studies in Mice. *J Nucl Med.* 2006:999-1006.

Physical & Performance Characteristics of Preclinical MuPET Camera

- MuPET is a high-resolution and high-sensitivity Preclinical PET/CT camera. It has been designed and constructed at the University of Texas MD Anderson Cancer Center.
- PET scanner is based on the low-cost photomultiplier-quadrant-sharing (PQS) concept and the high-precision and low-labor detector-block production method named slab-sandwich-slice (SSS) method.
- Camera is composed of 180 blocks of 13 x13 crystals (each: 1.24 x 1.4 x 9.5 mm^3) and 210 low-cost 19-mm diameter photomultipliers (R1450 – Hamamatsu).
- Camera has 78 detector rings with an 11.6-cm axial field of view and diameter of 16.6 cm.
- We have developed special low-noise and low-dead-time electronics for MuPET camera. Our homemade electronics include 210 gain-programmable PMT dividers, 1 analog pre-processing board, and 3 field-programmable gate array (FPGA)-based event-position decoding boards.
- PET detection system is a solid no-gap detector with PMTs directly coupled to blocks.
- Camera resolution is about 1.2 mm which improves to about 0.8 mm with a resolution recovery method and remains below 1.2 mm for the 6-cm central transaxial FOV region .
- Absolute sensitivity of the PET scanner is 6.4% for an energy window of 350-650 keV and a coincidence timing windows of 3.4 ns.
- NECR peak is 1100 (534) kcps for the NEMA mouse- (rat-) like phantom.

Images of Phantoms and Mice

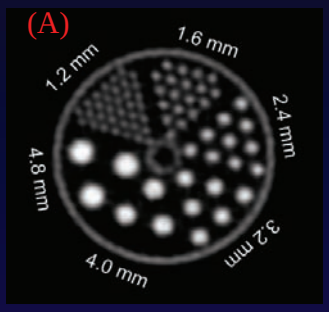

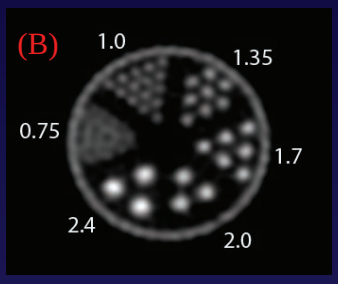

Images of Micro-Deluxe (A) and Ultra-Deluxe (B) phantoms (both phantoms from Data Spectrum Corp).

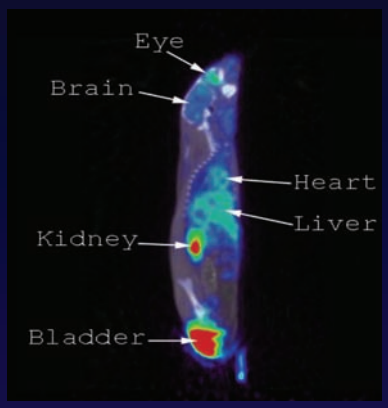

Sagittal PET image of a healthy mouse fused with CT image. Mouse was injected with 29 MBq of FDG and anesthetized with ketamine/xylazine/ atropine cocktail and scanned 2 h later.

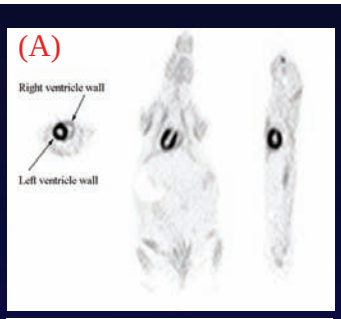

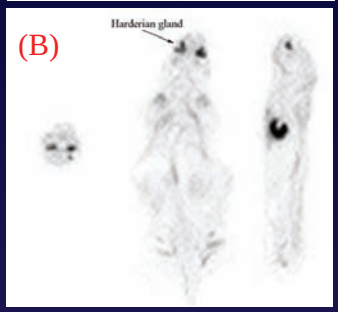

Non-gating images of a non-fasting healthy mouse. Mouse was injected with 17.4 MBq of FDG, anesthetized with isoflurane, and scanned 1 h later. The left- and –right ventricle walls (A) and the Harderian glands (B) are observable.

THE UNIVERSITY OF TEXAS
MD Anderson Cancer Center
Making Cancer History®

Enhanced Scintillation Crystals Through Co-Doping and Growth Improvements

Samuel Blahuta[a*], Vladimir Ouspenski[a], Daniel Herr[b], John Frank[b]

[a]*Saint-Gobain Recherche, 39 quai Lucien Lefranc, 93303 Aubervilliers Cedex, France*
[b]*Saint-Gobain Crystals, 17900 Great Lakes Parkway, Hiram, OH 44234, USA*

The scintillation properties of crystals, including LYSO and LaBr3, can be enhanced through co-doping and growth improvements. This paper will provide a status on the progress achieved and how these improvements directly apply to the requirements of PET, CT and other applications.

For example, LYSO ($Lu_{2(1-x)}Y_{2x}SiO_5$:Ce (10% at Y)) single crystals co-doped with Ca^{2+} and Mg^{2+} were shown to have improved scintillation performances (light yield, afterglow and energy resolution) [1]. For the first time it was also shown that co-doping LYSO with divalent elements leads to the stabilization of a significant part of the doping ions in their Ce^{4+} oxidation state. This consequence has no effect on the crystal aspect (e.g. coloration or self-absorption).

This current generation of LYSO crystals has been pushed further with a new developed concept using more oxidized conditions. In LYSO as in many oxides the main electronic defects are oxygen vacancies [2]. These vacancies can cause light yield decrease, afterglow and longer decay time [3]. In order to limit their formation during the growth more oxidizing conditions were used.

The scintillation performances of these new 3rd generation LYSO crystals which combine efficient co-doping together with oxidizing conditions significantly overpass the existing ones:

- The light yield is increased up to 135% of standard LYSO:Ce
- Decay time can be reduced by 16%
- Afterglow can be similar to the best commercially available GOS:Pr,Ce ceramics used for medical CT. The Figure below compares the afterglow of the different generations of LYSO.

Results showing similar scintillation performance enhancement for LaB3 will also be discussed.

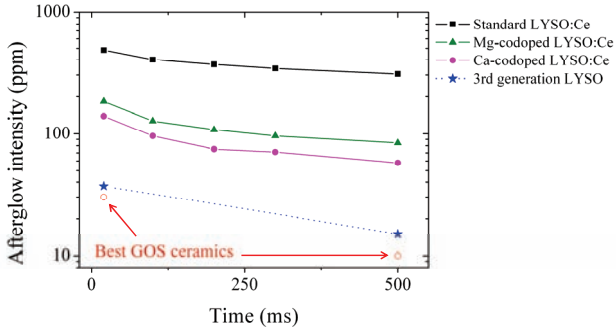

Figure 1: Afterglow after X-ray excitation at 300 K of LYSO:Ce single crystals from different generations. Afterglow of the best commercially available GOS:Pr,Ce ceramics is also represented.

* *corresponding author e-mail: daniel.j.herr@saint-gobain.com*

References

[1] Samuel Blahuta and Vladimir Ouspenski, "Low-afterglow co-doped LYSO:Ce" Oral presentation IEEE/NSS 2012, Anaheim, USA.

[2] Samuel Blahuta, Aurélie Bessière, Bruno Viana, Vladimir Ouspenski, Eric Mattmann, Julien Lejay and Didier Gourier, "Defects identification and effects of annealing on LYSO single crystals for scintillation application", Materials **4**, 1224-1237 (2011).

[3] Piotr Szupryczynski, Charles L. Melcher, Merry A. Spurrier, Michael P. Maskarinec, Andrew A. Carey, Andrzej J. Wojtowicz, Winicjusz Drozdowski, Darek Wisniewski and Ron Nutt, "Thermoluminescence and Scintillation Properties of Rare Earth Oxyorthosilicate Scintillators" IEEE Transactions On Nuclear Science **51**, n°3, 1103-1110 (2004).

Current Status

	Density	1 / μ (511 keV)	$\lambda_{emission}$ (nm)	Light Yield (ph/MeV)	Energy Resolution	Decay time
BGO	7.1	10.5 mm	480	8200	15%	300 ns
LuAP:Ce	8.3	10.6 mm	365	11000	9%	60 + 600 ns
LSO:Ce	7.4	11.5 mm	420	30000	9%	40 ns + afterglow
LYSO:Ce (10%Y)	7.1	12.2 mm	420	32000	8%	40 ns + afterglow

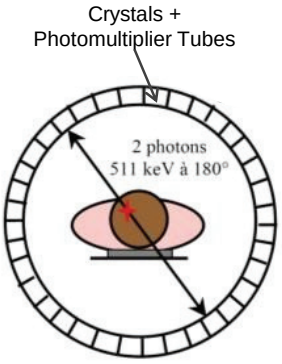

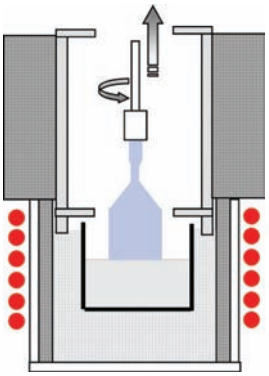

Czochralski growth

LYSO:Ce is an outstanding scintillator for PET

What if:

- **Light Yield is further improved?**
- **Decay time if made faster?**
- **Afterglow is made significantly lower?**

SAINT-GOBAIN CRYSTALS

Ca^{2+} / Mg^{2+} co-doping

- Improved Light Yield
  → up to 40000 Photons/MeV
- Improved decay time
  42 ns → 35 ns
- Improved Energy Resolution
- Improved Afterglow – enables CT

Composition	Std. LYSO	Gen3 LYSO with Ca	Gen3 LYSO with Mg
LY (Ph/MeV)	28000	36000	40000
Decay time	42 ns	35 - 36 ns	35 – 36 ns
Energy Res.	8.5%	7%	7%

3rd Generation LYSO

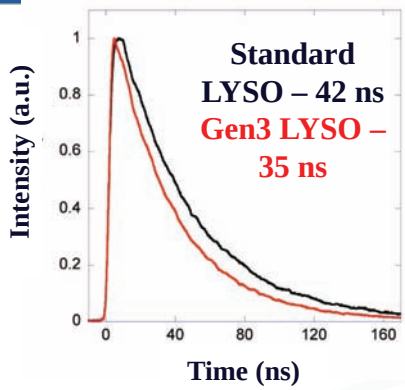

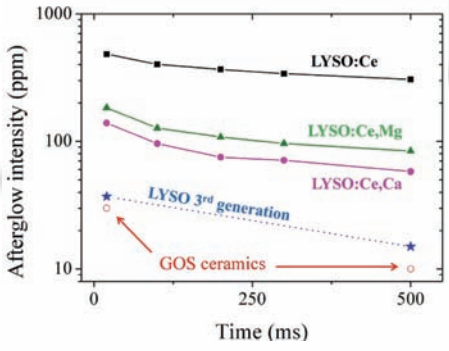

SAINT-GOBAIN CRYSTALS

VECTor^{+}: 1/4 mm, 1/4 minute & 1/4 MBq quantitative total body SPECT, with simultaneous 3/4-mm PET and 2/4-mm SPECT capability.

Freek Beekman[1,2], Oleksandra Ivashchenko[2], Frans van der Have[1,2], Rob Kreuger[1], Pieter Vaissier[1], Brendan Vastenhouw[1,2], Marlies Goorden[1]

[1]Section Radiation Detection and Medical Imaging TU-Delft, The Netherlands [2]MIlabs B.V. Utrecht, The Netherlands

Pivotal questions in pharmacology and biology concern how function of localized cells relates to disease. In experimental neuroscience we have dreamt about a magnifying glass that would allow us to see neurotransmitters in action, in cardiovascular research about a system that would simultaneously provide us with mechanical functions *and* various cell functions, and in cancer research about simultaneous dynamic high-resolution imaging of distributions of pharmaceuticals and indicators of tumor response. In recent years, many groups have been involved in the development of pinhole-SPECT systems for imaging rodents (van der Have *et al.*, 2009; Furenlid *et al.*, 2004). At MILabs and TU-Delft, an Ultra-high resolution Single Photon Emission Computed Tomography with integrated X-ray CT (U-SPECT^{+}/CT) has been developed that can quantify tracer dynamics in <1/4 mm structures by applying novel focusing multi-pinhole geometries together with new acquisition and reconstruction methods (Ivashchenko *et al.*). Recently, we also developed a new way to perform U-SPECT imaging simultaneously with sub-mm Positron Emission Tomography (PET). This Versatile Emission Computed Tomography system, dubbed VECTor (Goorden *et al.*, 2013), is based on clustered multi-pinhole technology..

We will show U-SPECT/CT and VECTor/CT images and movies that are recorded by world-wide users of these technologies. Examples include high-resolution imaging of glucose uptake and density and occupancy of transporters/receptors in the brain, ultra-high-resolution myocardial perfusion imaging, images of tumor marker and anti-cancer agents (e.g. antibodies) and beta cell imaging during a range of points in time. In addition, we will show examples of some new SPECT- and simultaneous SPECT/PET technologies which were recently developed by TU-Delft and MILabs.

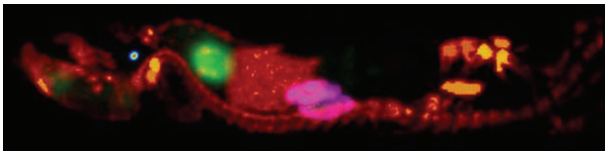

Figure 1. Simultaneous SPECT and PET isotope imaging with VECTor: maximum-intensity-projection of a 60 minute total-body mouse-scan with 100 MBq ^{99m}Tc-HDP (red), 35 MBq ^{18}F-FDG (green), 19 MBq ^{111}In-pentetreotide (magenta) and 5 MBq ^{123}I-NaI (rainbow).

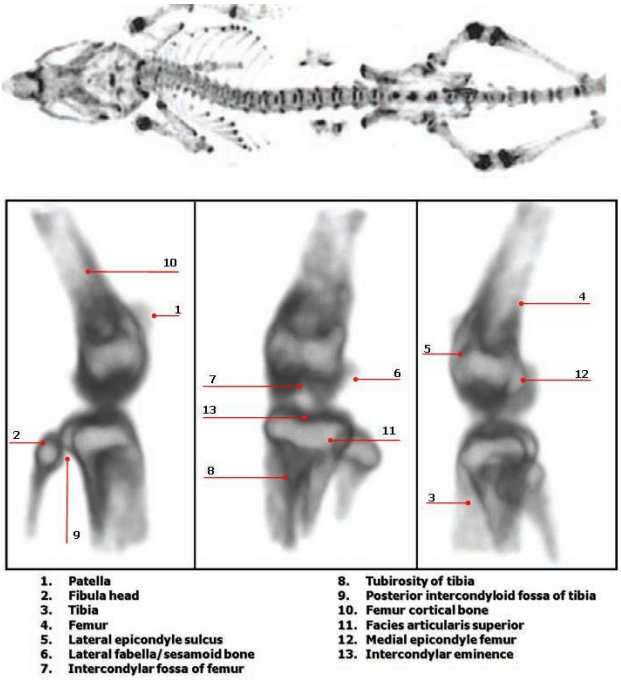

Figure 2. Quarter-mm resolution U-SPECT bone-scan of a mouse, with anatomical details provided of mouse knee

References

Furenlid L R, Wilson D W, Chen Y C, Kim H, Pietraski P J, Crawford M J and Barrett H H 2004 FastSPECT II: A second-generation high-resolution dynamic SPECT imager IEEE Transactions on Nuclear Science **51** 631-5

Goorden M C, van der Have F, Kreuger R, Ramakers R M, Vastenhouw B, Burbach J P H, Booij J, Molthoff C F M and Beekman F J 2013 VECTor: A Preclinical Imaging System for Simultaneous Submillimeter SPECT and PET Journal of Nuclear Medicine **54** 306-12

Ivashchenko O, van der Have F, Villena J and Beekman F Quarter millimeter resolution pre-clinical SPECT with quarter-mm pinholes European Journal of Nuclear Medicine and Molecular Imaging

van der Have F, Vastenhouw B, Ramakers R M, Branderhorst W, Krah J O, Ji C G, Staelens S G and Beekman F J 2009 U-SPECT-II: An Ultra-High-Resolution Device for Molecular Small-Animal Imaging Journal of Nuclear Medicine **50** 599-605

^{99m}Tc-HDP bone-scan of mouse knee with VECTor^{+}

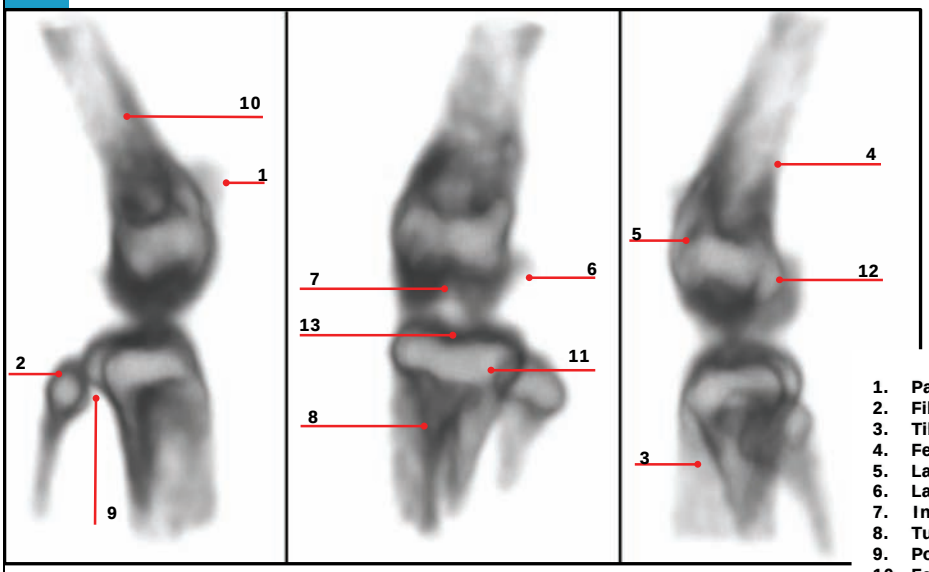

1. Patella
2. Fibula head
3. Tibia
4. Femur
5. Lateral epicondyle sulcus
6. Lateral fabella/sesamoid bone
7. Intercondylar fossa of femur
8. Tubirosity of tibia
9. Posterior intercondyloid fossa of tibia
10. Femur cortical bone
11. Facies articularis superior
12. Medial epicondyle femur
13. Intercondylar eminence

Ivashchenko O, van der Have F, Villena J, Beekman FJ.
Quarter millimeter resolution pre-clinical SPECT with quarter-mm pinholes.
Eur J Nucl Med Mol Imaging., In Press.

TUDelft MILabs

Simultaneous multi-isotope SPECT-PET imaging

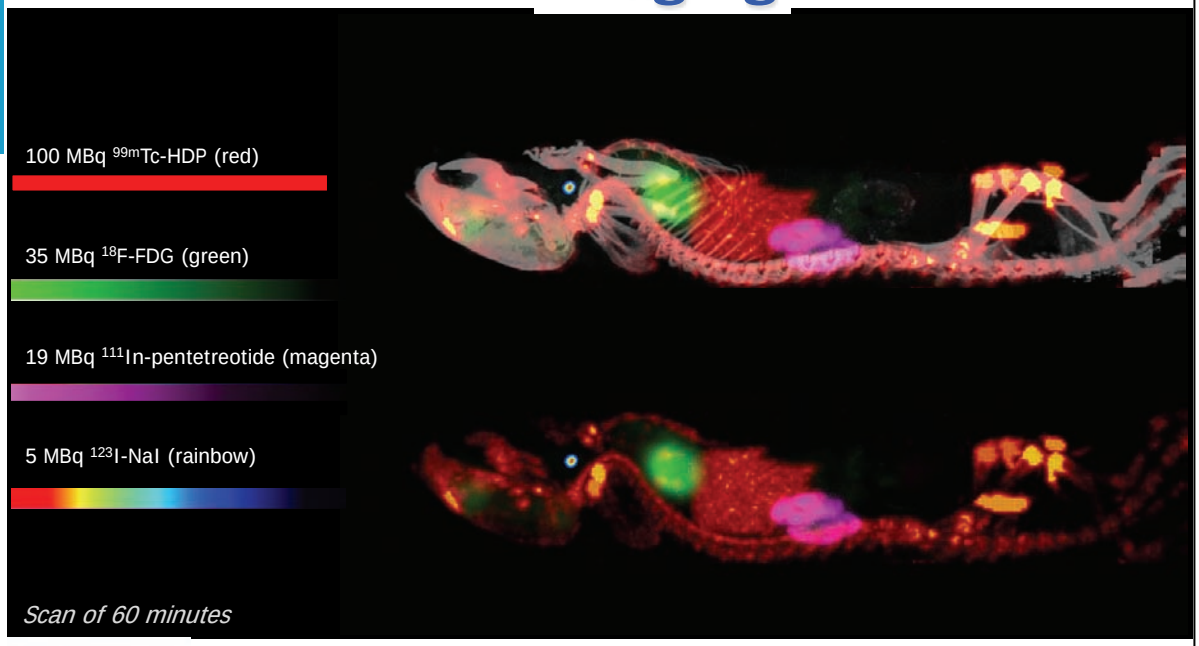

M.C. Goorden et al.
VECTor: A Preclinical Imaging System for Simultaneous sub-mm SPECT and PET.
J.Nucl.Med., 2013.

TUDelft MILabs

Development of molecular imaging systems and applications

Seiichi Yamamoto[1]

[1] Nagoya University Graduate School of Medicine, Japan, s-yama@met.nagoya-u.ac.jp

We have developed two optical fiber based integrated PET/MRI systems for small animals [1-2] and two Si-PM based PET systems [3-4] that can be combined with MRI systems. There are some advantages and disadvantages in optical fiber based and Si-PM based PET/MRI systems. The main advantage of the optical fiber based PET system is less or no interferences between PET and MRI and the disadvantage is the light loss of the fiber which degrades the performance of the PET. The advantage of the Si-PM based PET system is no light loss and the disadvantages are the interferences between PET and MRI [5-6] and the temperature dependent sensitivity changes [7]. From our experiences, optical fiber PET systems are suitable for combined with low magnetic field MRI systems because the signal level of these MRI systems are small and sensitive to the noise from PET systems. Si-PM PET systems are suitable for higher magnetic field MRI systems probably because the signal level is higher enough to ignore the noise from the PET systems although some interference from RF and gradient signals may decrease the performance of the Si-PM PET systems.

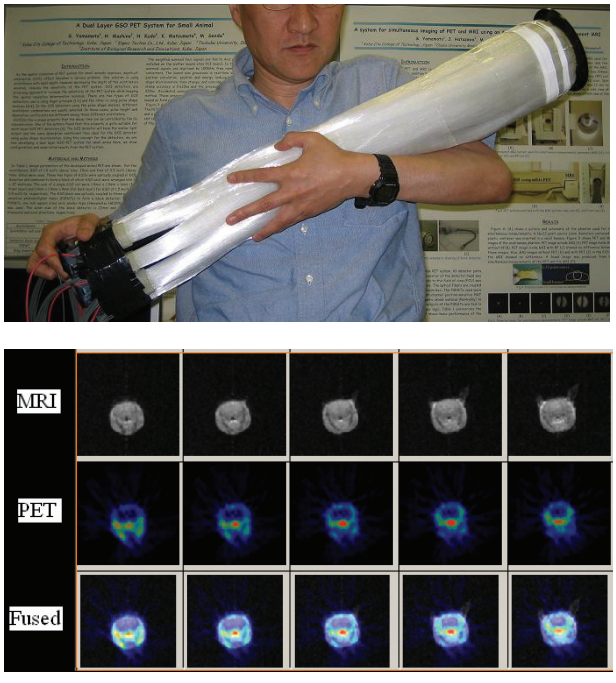

Fig. 1 High resolution optical fiber based PET/MRI system (upper) and simultaneously measured mouse images with optical fiber based PET/MRI system (lower)

One of our optical fiber based PET system [2] employed 0.5mm diameter double clad fibers and are optically coupled to position sensitive photomultiplier tubes. A 0.3T open-MRI is combined with the optical fiber PET system. Figure 1 shows a photograph of the optical fiber based PET/MRI system and simultaneously measured mouse images. The spatial resolution of the integrated PET system was 1.2mm and sensitivity was 1.2%, better than one of the Si-PM PET systems we developed [2]. So we still feel optical fiber based PET systems are promising for new hybrid systems in which the interference with other modality is critical. Si-PM PET systems are promising for combining with high field MRIs but we need to minimize the interference between PET and MRI for both modalities.

In addition, Si-PM array is a good material to achieve ultrahigh resolution PET system with small size channels. Using Si-PM arrays combined with 0.5mm size LYSO pixels, we could develop a small animal PET system with 0.7mm resolution [4]. We show the developed Si-PM based ultrahigh resolution PET system and mouse images in Fig. 2. With this PET system, ultrahigh resolution PET/MRI system will also be realized.

We are now planning two new integrated systems for small animals, one is optical fiber based and the other is Si-PM based.

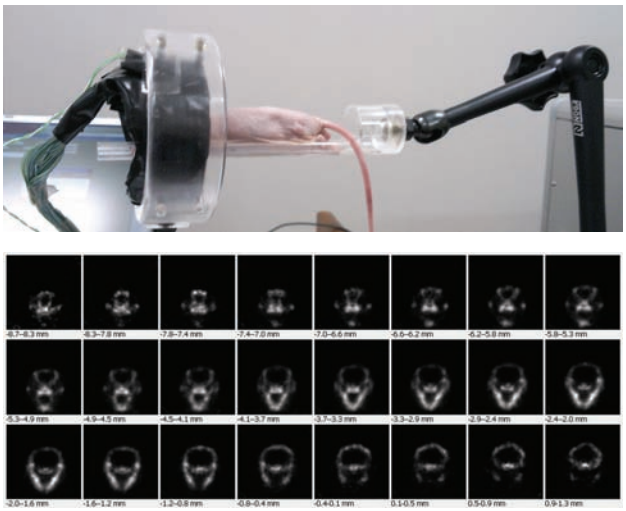

Fig. 2 Si-PM based ultrahigh resolution PET system (upper) and measured F-18-NaF mouse images (lower)

References

[1] S. Yamamoto, et al. Ann. Nucl. Med. ; 24(2):89-98, 2010
[2] S. Yamamoto, et al. Med. Phys.; 39(11): 6660-6671, 2012
[3] S. Yamamoto, et al. Phys. Med. Biol.; 55(19):5817-31, 2010
[4] S. Yamamoto, et al. Phys. Med. Biol., in-press
[5] S. Yamamoto, et al. Phys. Med. Biol.; 56(13):4147-59, 2011
[6] S. Yamamoto, et al. Phys. Med. Biol.; 57(2):N1-13, 2012
[7] S. Yamamoto, et al. Phys. Med. Biol. 56; 2873-2882, 2011

High resolution optical fiber based PET/MRI system

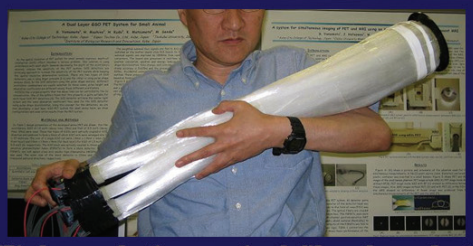

High resolution optical fiber based MR-compatible PET

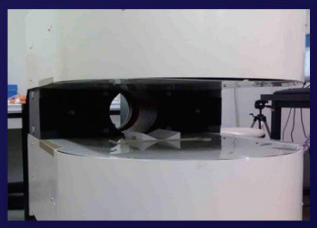

0.3T MRI with hole in yoke

Combine

2 types of LGSOs (31ns & 46ns) for DOI detector
0.5mm diameter optical fiber bundle (75cm long)

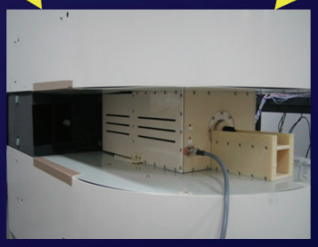

High resolution integrated PET/MRI

Mouse brain NaF-18 (F-minus)

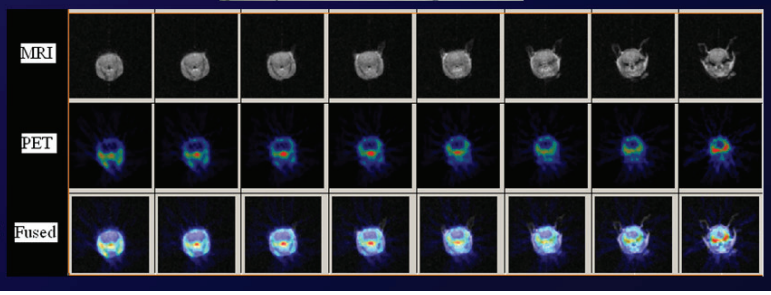

Silicon Photomultiplier (Si-PM) based UHR-PET detector

Block detector for UHR PET

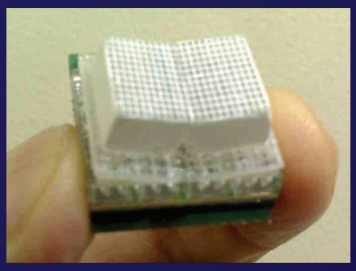

Two LYSO blocks were optically coupled to a Si-PM array with angled optical fiber light guides. LYSO pixel size: 0.5mm x 0.7mm x 5mm

UHR-PET detector ring

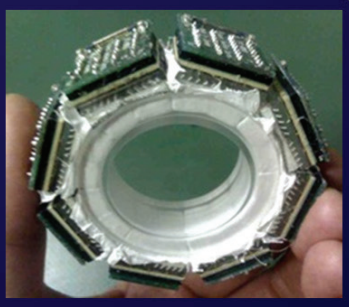

Eight block detectors were arranged in 34mm diameter ring.

Developed UHR PET system
Spatial resolution: 0.75mm

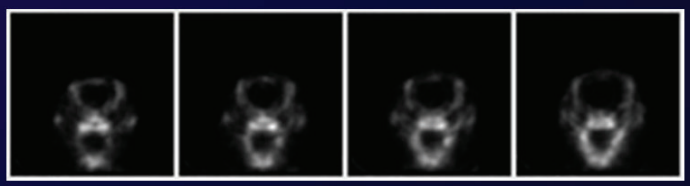

High resolution mouse brain (F-18-NaF)

Development of a removable MR head coil integrated with high-resolution PET detectors

Takayuki Obata, Mikio Suga*, Fumihiko Nishikido, Atsushi Tachibana, Koudai Shimizu*, Hiroshi Kawaguchi, Taiga Yamaya

National Institute of Radiological Sciences, Chiba, Japan, t_obata@nirs.go.jp

*Graduate School of Engineering, Chiba University, Chiba, Japan

BACKGROUND and GOAL

Recently, PET-MRI systems have become available for clinical use, and they have provided much useful information. However, because PET detectors are located near the MRI gantry, spatial resolution is difficult to improve.

A depth-of-interaction (DOI) detector, developed in our institute, enables us to set PET detectors near the local RF coil and get high-quality PET images with higher spatial resolution.

If a compact RF coil integrated with PET detectors could be developed, we could obtain not only high-quality images but also have capability and removability added to PET-MRI systems. The problem with integration of PET detectors for the RF coil is that the interaction between RF coil, PET detectors, and shield boxes packing the detectors will be stronger.

The purpose of this study is to develop a compact RF coil integrated with PET detectors and evaluate the interaction of the shield boxes and PET detectors with MRI as a preliminary study.

METHODS

Development of an RF coil for a compact PET-MRI system

A birdcage-type RF coil was selected because it is easy to set PET detectors between the coil elements and because RF irradiation to PET detectors can be reduced by transmitting and receiving mode. Tuning and matching adjustments were done after eight copper shield boxes were set between the coil elements.

Interaction of shield boxes with MR images To evaluate the effect of the shield boxes on B0 and B1, the homogeneity of B0 maps and modulus spin echo images in a water phantom were calculated. A gradient echo sequence with a strong magnetic gradient preparation was used to measure the phase shift induced by eddy current.

Interaction between MRI and PET signals We also carried out experiments with the RF coil and the four-layer DOI detector. Only one detector was mounted in one shield box of the RF coil.

RESULTS

We succeeded in making a birdcage-type coil with attached eight shield boxes for PET detectors (Fig.1). Tuning and matching were well adjusted to the resonance frequency of proton at 3T.

The same quality of B0 and B1 homogeneities with shield boxes as those without shield boxes was obtained. The eddy current-induced phase shift from the shield boxes was much smaller than that from other equipment using this method.

No significant degradations of the performance of the PET detector and MR images in simultaneous measurements were observed.

CONCLUSION

We developed a compact RF coil with attached eight shield boxes for PET detectors, and obtained successful results in a preliminary trial.

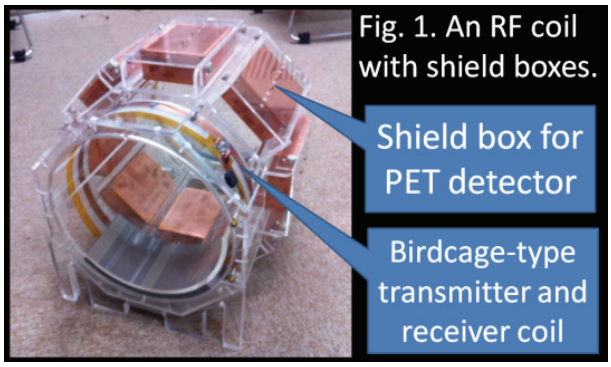

Fig. 1. An RF coil with shield boxes.

A removable MR RF coil integrated with high-resolution PET detectors

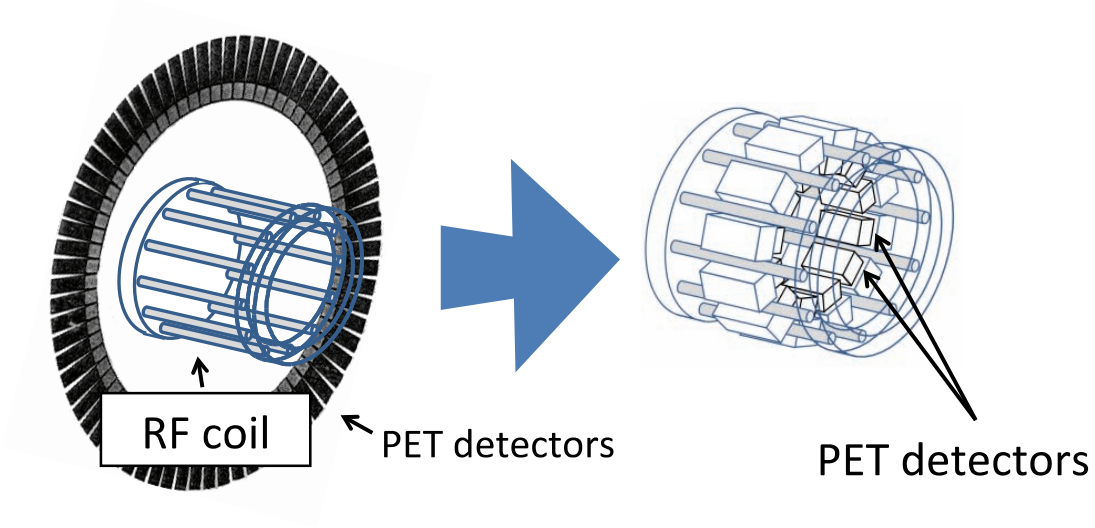

RF coil with shield boxes

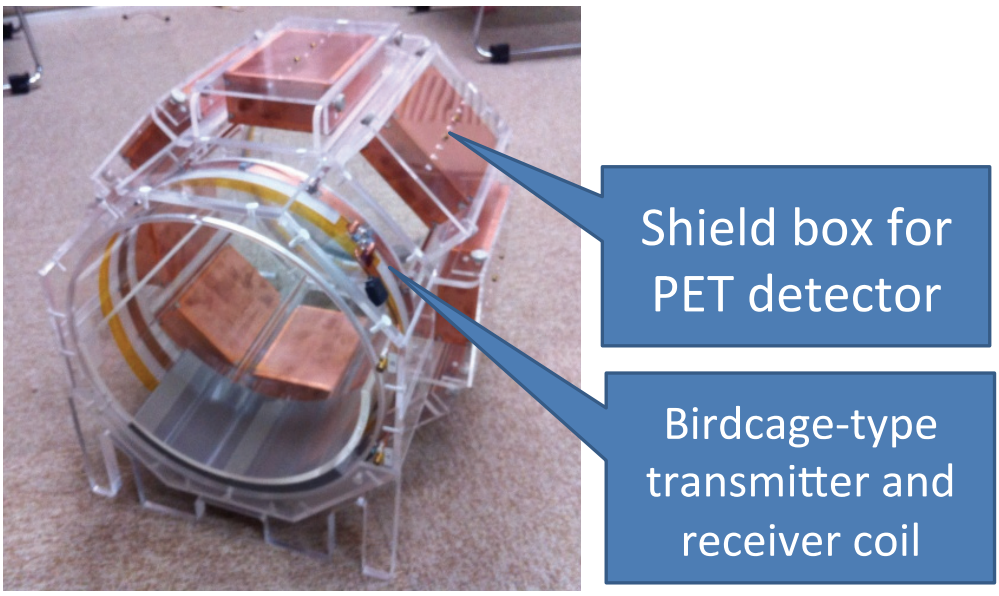

First experience with a novel Preclinical PET/CT scanner with stationary/rotating detectors

Nicola Belcari[1,2], Daniele Panetta[3],Niccolò Camarlinghi[1,2], Matteo Cecchetti[1], Elena Fabbiani[1,2], Stefano Ferretti[1,2], Patricia Iozzo[3], Piero A. Salvadori[3], Giancarlo Sportelli[1,2] and Alberto Del Guerra[1,2], *IEEE Fellow*

[1] Department of Physics "E. Fermi", University of Pisa and INFN Pisa, Italy, belcar@df.unipi.it ,[2] INFN Pisa, Italy, [3] CNR Institute of Clinical Physiology, Pisa, Italy

1. Introduction

A novel preclinical PET/CT system for mice and rats has been developed featuring state of the art technology. The scanner comprises a full ring PET and a high resolution CT system placed sequentially like in clinical PET/CT scanners. The scanner has a high sensitivity of 8.2% at CFOV (350-750 keV energy window) and a high spatial resolution. The optimized PET detector module design allows to reach and excellent energy resolution of about 14%. This work presents the performance of the system and the effect on image quality of the unique feature of the PET component, together with the first results obtained with phantoms, mice and rats (fig 1).

2. System design

The PET component of the scanner consists of 16 modular detectors arranged in two octagonal rings. The field-of-view has 95 mm axial coverage and a diameter of 80 mm. Each module comprises a lutetium-yttrium orthosilicate:cerium (LYSO:Ce) matrix of 702 crystals of 1.6 mm × 1.6 mm × 12 mm with a pitch of about 1.7 mm directly coupled to a 64 anodes PMT (Hamamatsu H8500).

The front-end electronics for the readout of the 64 channels of the H8500 PMT is based on a dedicated active resistive charge divider [1]. Timing signals (one for module) are produced with constant fraction discriminators acting on the last dynode signal. Both position and last dynode signals are conditioned by fast pre-amplifier with the aim of minimizing dead time.

Acquisition electronics is based on short deadtime pulse discriminators, a series of peak detectors for position and energy acquisition and a synchronous coincidence processor operating at 288 MHz with a coincidence window of 5.2 ns [2] and it is connected to the acquisition PC via USB.

The PET system also feature the unique possibility to perform rotational acquisitions where data are acquired at several angular positions while the PET ring spins around the object (step-and-shoot mode). Images can be reconstructed with LOR based 3D ML-EM with multi-ray-based system matrix [3]. Attenuation correction is performed with CT-based μ-maps.

The CT system comprises a 3 MPixel CMOS detector (75 μm pixel pitch) coupled to 150 μm CsI scintillator and a 80 kV X-ray source with 50 μm focal spot size. CT images are reconstructed with a Feldkamp-type FBP.

3. Results and conclusions

The novel PET/CT scanner shows to be optimized for high speed imaging having a very high sensitivity for PET imaging and fast CT system.

Even if not strictly necessary in this case due to the full angular coverage of the detectors, the results obtained in rotational mode show a significant reduction in the image noise in comparison to the non-rotational thus making this acquisition mode particularly well suited for those cases where image quality is more important than the tracer dynamic information.

The overall measured performance and the unique features make this new system a powerful but also cost-effective solution for pre-clinical research on mice and rats.

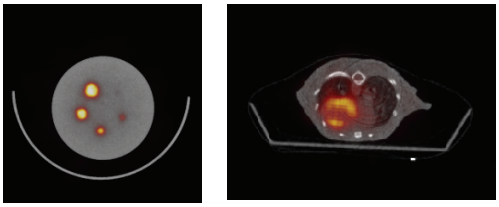

Figure 1: very first images obtained with the new PET/CT system in non rotational PET mode. Left: image quality phantom, right: mouse with 18F-FDG. Both images have been obtained in less that 6 min. including PET and CT

References

[1] N. Belcari et al., Performance of a four-output front-end electronics for multi-anode PMTs readout of scintillator arrays, Nuclear Instruments and Methods in Physics Research Section A 572 (2007) 335–337

[2] G. Sportelli, et al., Nuclear Instruments and Methods in Physics Research Section A 648 (S1) (2011)

[3] S. Moehrs et al. Multi-ray-based system matrix generation for 3D PET reconstruction, Phys. Med. Biol. 53 (2008) 6925–6945

First experience with a novel Preclinical PET/CT scanner w stationary/rotating detectors

Nicola Belcari[1,2], Daniele Panetta[3],Niccolò Camarlinghi[1,2], Matteo Cecchetti[1], Elena Fabbiani[1,2], Stefano Ferretti[1,2], Patricia Iozzo[3], Piero A. Salvadori[3], Giancarlo Sportelli[1,2] and Alberto Del Guerra[1,2]

1) Department of Physics "E. Fermi", University of Pisa and INFN Pisa, Italy 2) INFN Pisa, Italy, 3) CNR Institute of Clinical Physiology, Pisa, Italy

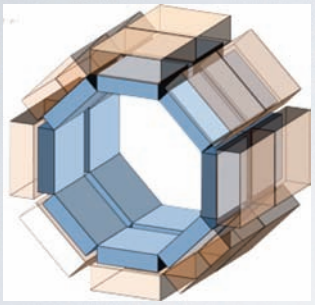

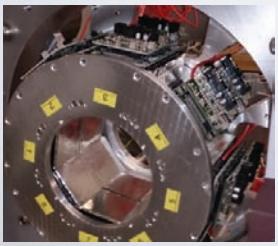

Detector module specifications	
Crystal material	LYSO:Ce
Crystal size (mm)	1.60 mm x 1.60 mm
Crystal pitch (mm)	1,70 mm
Crystals per module	27 x 26
Photodetector	MA-PMT 64 ch.
System specifications	
No. of modules	16
No. of rings	2
Bore size (mm)	100 mm
FOV size (mm)	80 mm (T) x 95 mm (A)
Other features	
Detector rotation	up to 360°

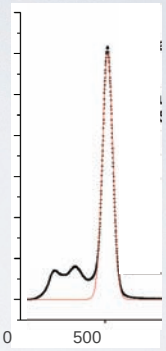

System energy resolution: <14% FWHM @ 511 keV

Sensitivity:

Maximum absolute sensitivity @ CFOV

- 9.8% (250-750 keV)
- 8.1% (350-750 keV)

PET design and picture of the PET ring.

SYSTEM PERFORMANCE

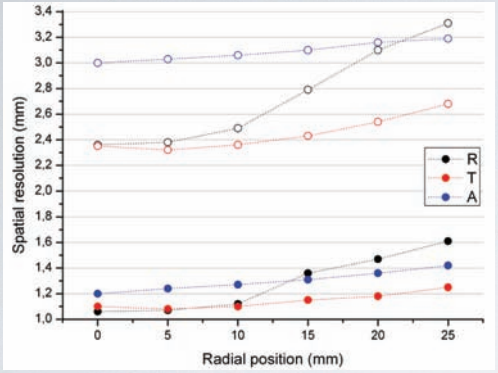

Spatial resolution : FWHM (solid) and FWTM (empty) in the central plane (3D ML-EM reconstruction, 15 iterations)

Static vs rotating acquisitions

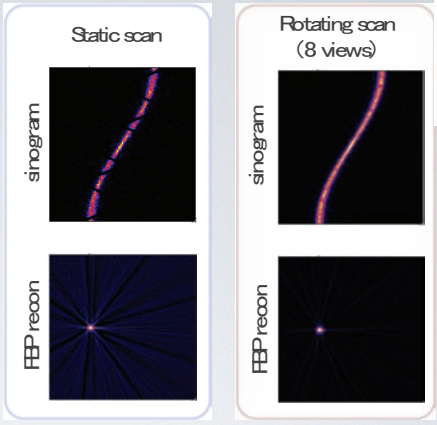

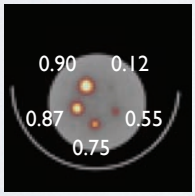

PET/CT transaxial image of the NEMA NU-4 2008 image quality phantom and measured recovery coefficients

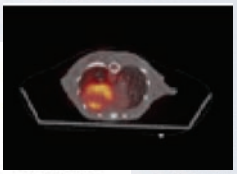

[18F-FDG)/CT of a mouse
tal scan time < 6 min.

To be commercialized by INVISCAN with the brand name IRIS PET/CT

NIRS Workshop on PET Imaging Physics and Applications PIPA2013 Abstract Book

Date of Publishing: November 4, 2013

Editing and Publication:

Taiga Yamaya

Molecular Imaging Center, National Institute of Radiological Sciences

4-9-1 Anagawa, Inage-ku, Chiba 263-8555, Japan

e-mail : jpet@nirs.go.jp

Printed in Japan

NIRS-M-261